

1 **Increasing precipitation due to climate change could partially**
2 **offset the impact of warming on glacier loss in the monsoon-**
3 **influenced Himalaya until 2100 CE**

4
5 Anya M. Schlich-Davies^{1*}, Ann V. Rowan^{2*}, Andrew N. Ross¹, Duncan J. Quincey³, Vivi K.
6 Pedersen⁴

7
8 ¹Priestley International Centre for Climate, School of Earth and Environment, University of Leeds,
9 UK

10 ²Department of Earth Science, University of Bergen and Bjerknes Centre for Climate Research,
11 Bergen, Norway

12 ³School of Geography, University of Leeds, UK

13 ⁴Department of Geoscience, Aarhus University, Aarhus C, Denmark

14
15 *These authors contributed equally to this work

16
17 Correspondence to: Ann V. Rowan (ann.rowan@uib.no)

18
19
20 **Abstract.** Glacier **mass** in the Himalaya is projected to shrink by 53–70% due to climate change **by**
21 **2100 CE**. However, the impact of changes in precipitation amount and distribution on future glacier
22 change remains uncertain because mesoscale meteorology is not represented in current glacier **models**.
23 We **explored** the combined effects of past and future changes in air temperature and precipitation
24 amount and distribution on the evolution of Khumbu Glacier in the Everest region of Nepal. **We used a**
25 **climate-glacier modelling approach that forced** an ice-dynamical glacier evolution model with surface
26 mass balance forcings that **included** mesoscale meteorological variables derived from downscaling of
27 Regional Climate Model results. Our simulations show **that** historical warming has committed Khumbu
28 Glacier to future **mass** loss of 10–23% during this century, and that under an intermediate future
29 emissions scenario (RCP4.5), Khumbu Glacier could lose 70% **mass** by 2100 CE due to warming.
30 However, the projected increase in precipitation in tandem with warming could offset about half of the
31 projected glacier loss, such that the total decrease in glacier **mass** by 2100 CE compared to the present
32 day **would be reduced to** 34%. Under a high future emissions scenario (RCP8.5) glacier loss due to
33 warming will not be compensated by changes in precipitation, but will instead result in substantial
34 ablation above 6,000 m **with devastating consequences for one of the highest glaciers on Earth**.

35
36 **1. Introduction**

37 Projecting glacier **mass** change in response to climate change is important for determining the impact
38 of anthropogenic warming on regional water availability (Pritchard, 2019). High Mountain Asia is
39 projected to lose $34 \pm 19\%$ of glacier **mass** by 2100 CE if warming is limited to 1.5°C to meet the
40 ambitious Paris Agreement target (Kraaijenbrink et al., 2017). **Less ambitious** projections give $53 \pm$
41 23% **glacier mass** loss by 2100 CE under the intermediate emissions scenario RCP4.5, and $69 \pm 20\%$
42 under the high emissions scenario RCP8.5 (Kraaijenbrink et al., 2017; Marzeion et al., 2020; Rounce
43 et al., 2023). **However, such** projections are **challenging to make** because accumulation and ablation
44 processes in mountain environments are driven by orographic feedbacks between high-relief
45 topography and atmospheric circulation systems such as the South Asian Summer Monsoon
46 (Bookhagen and Burbank, 2006). Furthermore, large uncertainties arise from the challenge of
47 simulating the interactions between the mass balance regimes of monsoon-influenced glaciers, where
48 accumulation and ablation both occur during the monsoon season, and the dynamics of glaciers flowing
49 through high-relief topography, **that includes processes** such as the development of supraglacial debris
50 layers that modify surface melting (Dehecq et al., 2019; Miles et al., 2018b; Salerno et al., 2023).
51 Variability in the extent and intensity of the Indian Summer Monsoon during the Last Glacial Maximum
52 affected glacier expansion **in** the monsoon-influenced Himalaya through changes in snowfall
53 distribution (Benn and Owen, 1998; Owen et al., 2009). Future Indian Summer Monsoon precipitation

Formatted: Font colour: Auto

Deleted: volume

Deleted: by 2100 CE

Deleted: models of

Deleted: change

Deleted: explore

Deleted: —

Deleted: benchmark glacier in the monsoon-influenced Himalaya—using a ...

Deleted: forces

Deleted: includes

Deleted: volume

Deleted: volume

Deleted: volume

Deleted: is only

Deleted: that causes Khumbu Glacier to vanish by 2160–2260 CE...

Deleted: volume

Deleted: More realistic

Deleted: of glacier change

Deleted: volume

Deleted: Such

Deleted: ,

76 and variability projected in Global Circulation Models (GCMs) will increase with current global
77 warming (Katzenberger et al., 2021), but the effect of projected changes in precipitation amount, timing,
78 and phase (rain/snow) on Himalayan glaciers remain poorly constrained (Immerzeel et al., 2012; Mölg
79 et al., 2014; Ragettli et al., 2016; Shaw et al., 2022; Shea et al., 2015).

81 Supraglacial debris covers 4–7% of glacier surfaces globally and 30% of glacier ablation areas in the
82 Himalaya, and modifies the response of glaciers to climate change relative to regional trends (Herreid
83 and Pellicciotti, 2020; Kraaijenbrink et al., 2017; Rounce et al., 2023; Rowan et al., 2015). Satellite
84 observations show that the rate of glacier mass loss across the Himalaya has accelerated over the last
85 40 years for both clean-ice glaciers and debris-covered glaciers (Maurer et al., 2019). Observations and
86 modelling studies indicate that thick supraglacial debris caused historical mass loss from debris-covered
87 glaciers to lag that of clean-ice glaciers, such that debris-covered glaciers are currently larger than would
88 otherwise be the case (King et al., 2020; Rounce et al., 2023; Rowan et al., 2021). However, the
89 dampening effect of supraglacial debris on glacier mass loss is overturned by the development of
90 extensive supraglacial ponds and ice cliffs within debris layers (Miles et al., 2018a; Strickland et al.,
91 2023) and the stagnation and detachment of debris-covered tongues from the upper and more active
92 sections of glaciers (Rowan et al., 2021). Quantifying the impact of feedbacks set up by the formation
93 and expansion of supraglacial debris layers at a regional scale requires exploring these processes at
94 scales that can be resolved in ice-dynamical glacier evolution models (Rowan et al., 2015; Nicholson
95 et al., 2021; Compagno et al., 2022). These processes can be considered in 2-D (along the glacier
96 flowline) either considering stochastic debris delivery to the glacier (Vacco et al., 2010; Wirbel et al.,
97 2018) or continuous debris delivery, which can result in the over-accumulation of debris at the terminus
98 (Anderson and Anderson, 2016; Ferguson and Vieli, 2020; Jouvet et al., 2011), or in 3-D (using the
99 horizontal and vertical ice flow fields), which allows the lateral transport and deposition of debris to
100 the margins of the ablation area (Rowan et al., 2015).

102 While recent rapid warming resulted in a rise in regional equilibrium line altitude (ELA), that caused
103 recession and collapse of glacier termini for both clean-ice glaciers and debris-covered glaciers, the
104 decay of the former ablation areas of debris-covered glaciers is relatively delayed by supraglacial debris,
105 such that the terminus of the actively flowing glacier can remain in contact with the detached ice tongue
106 rather than separating (Maurer et al., 2019; Pellicciotti et al., 2015; Rowan et al., 2021). In common
107 with most large debris-covered Himalayan glaciers, Khumbu Glacier in the Everest region of Nepal is
108 in greater imbalance with climate than a climatically equivalent clean-ice glacier, and has maintained a
109 more extensive ice volume than would be possible without supraglacial debris (Rowan et al., 2021).
110 However, as a result of reduced ice flux from the accumulation area, the debris-covered tongue no
111 longer receives much (or any) input of ice, and has dynamically detached from the active glacier (Fig.
112 1c); this observation is confirmed by the rapid reduction in ice flow and the peak in glacier surface
113 lowering below the Khumbu Icefall where the debris layer is thinnest (King et al., 2020; Quincey et al.,
114 2009). Therefore, the active glacier and the stagnant debris-covered tongue will evolve along different
115 trajectories, and only the part of Khumbu Glacier above the terminus of the active glacier can be
116 considered dynamic (Fig. 1). Projections of future glacier evolution should therefore discount the
117 heavily debris-covered former tongue, which is decaying in situ without any input of new ice from the
118 accumulation area, while considering the development of supraglacial debris across the ablation area of
119 the active glacier.

121 We applied a novel glacier-climate modelling approach to Khumbu Glacier to test the hypothesis that
122 changes in precipitation in response to climate change will reduce the impact of warming on glacier
123 mass loss. Khumbu Glacier is a benchmark debris-covered glacier in the monsoon-influenced Himalaya
124 flowing from 7,981 m above sea level (a.s.l.) to 4,879 m a.s.l. that is representative of the majority of
125 glaciers in this region (Fig. 1). We used a 3-D ice-flow model forced by mass balance calculated from
126 mesoscale meteorological variables to simulate the evolution of Khumbu Glacier from the late
127 Holocene (~1 ka) through the present day (2015 CE) until 2100 CE using results from three downscaled
128 Regional Climate Models (RCMs) under two Relative Concentration Pathways (RCPs). This approach
129 represents an advance in the use of such models to understand the evolution of Himalayan glaciers, for
130 the first time mesoscale meteorological forcing is used with a climate-glacier model that represents the

Deleted: is

Deleted: by

Deleted: to

Deleted: on Himalayan glacier volume

Deleted: /rain)

Deleted: acts to modify glacier

Deleted: from

Deleted: glacier models

Deleted: has

Deleted: net

Deleted: melt

Deleted: now being

Deleted: Models of debris-covered glacier evolution represent the dynamic feedback between debris transport, mass balance and ice flow that differentiates the evolution of glaciers with a substantial supraglacial debris layer from climatically-equivalent clean-ice glaciers (Zekollari et al., 2022). Such models require numerical representation of the processes controlling debris delivery to glacier surfaces from hillslope erosion, englacial transport of debris through the glacier to accumulate at the ice surface in the ablation area, and the impact of an evolving supraglacial debris layer on surface melting (Nicholson et al., 2021).

Deleted: The high proportion of debris-covered glaciers in the monsoon-influenced Himalaya could significantly affect regional glacier change, and yet few studies currently consider the impact of supraglacial debris on glacier mass balance because impact of supraglacial debris on glacier change remains challenging to simulate at a regional or global scale (Compagno et al., 2022; Nicholson et al., 2021; Rounce et al., 2023). Glacier models at these scales treat supraglacial debris as static and do not yet account for the dynamic evolution of debris thickness and distribution in response to changes in mass balance and ice flow. Quantifying the impact of feedbacks set up by the formation and expansion of supraglacial debris layers at a regional scale requires exploring these processes at scales that can be resolved in ice-dynamical glacier evolution models (Rowan et al., 2015). While recent rapid warming resulted in a rise in regional equilibrium line altitude causing

Deleted: by the insulation of the ice surface

Deleted: (Fig. 1)

Deleted: .

Deleted: that

Deleted: use

Deleted: model of

Deleted: use

Deleted: glacier

Deleted: , as

180 processes of sublimation, snow avalanching, and debris transport, all of which are important controls
181 on the mass balance of Himalayan glaciers. Simulations start from the late Holocene when Khumbu
182 Glacier was last in dynamic equilibrium with the local climate, as evidenced by large ice-marginal
183 moraines dated to 1.3 ± 0.1 ka surrounding the present-day glacier (Hornsey et al., 2022), and when the
184 glacier surface was free of debris (Rowan et al., 2015). The focus of our experiments is to simulate
185 glacier evolution to the end of the 21st Century. However, the centennial dynamic response time of a
186 large debris-covered glacier such as Khumbu Glacier means that the glacier continues to evolve beyond
187 this time scale, and we continued the simulations until 2300 CE to explore longer-term glacier
188 evolution, albeit with greater uncertainties associated with results beyond 2100 CE.

190 2. Climate-glacier modelling of Khumbu Glacier

191 The climate-glacier glacier model experiments used mesoscale meteorological variables at an
192 appropriate scale to calculate surface mass balance for the Khumbu Glacier catchment in combination
193 with a debris-covered glacier evolution model to represent the surface processes that modify mass
194 balance. Our approach produced a total of six simulations of Khumbu Glacier from three CORDEX
195 South Asia region RCMs (NOAA, CCCma, IPSL; Lutz et al., 2016) and two RCPs (RCP4.5 and
196 RCP8.5; Collins et al., 2013) to explore the impacts of possible variability in future precipitation amount
197 and distribution in tandem with warming on glacier evolution. Before we use the RCMs to force the
198 future climate scenarios, we evaluated their capabilities against observations of present-day weather
199 and climate. The experimental design represents an advance compared with previous climate-glacier
200 modelling efforts by including robust representations of: (1) mesoscale meteorological phenomena,
201 including sublimation, (2) the redistribution of surface mass balance by snow avalanching, and (3) the
202 feedbacks between debris transport, ice flow and mass balance. This section describes the experimental
203 design for the climate-glacier modelling workflow (Fig. 2); a description of the study site, downscaling
204 of the present-day RCMs using meteorological data from automatic weather stations in the Khumbu
205 Valley, downscaling of the future RCMs for both RCPs, the surface energy and mass balance
206 calculations using COSIPY, and the debris-covered glacier evolution modelling using iSOSIA.

207 Khumbu Glacier (RGI2000-v7.0-G-15-08331) is 16.0 km long with an area of 26.4 km². The median
208 glacier elevation is 6,025 m a.s.l., from the terminus at 4,879 m a.s.l. to the headwall at 7,981 m a.s.l.
209 (RGI 7.0 Consortium, 2023). The stagnant debris-covered tongue has an area of 6.2 km² (23% of the
210 total glacier). The 'Little Ice Age' (LIA) maximum of Khumbu Glacier occurred about 500 years before
211 present, which is consistent with ages produced for moraines elsewhere in the central Himalaya
212 (Hornsey et al., 2022; Rowan, 2017). Khumbu Glacier was slightly larger than today during the late
213 Holocene, transitioning from a clean-ice glacier with high velocities and efficient export of debris to an
214 debris-covered glacier with lower velocities during the LIA; this change was initiated by the reduction
215 in ice flux promoted by a rise in ELA and thickening supraglacial debris (Rowan et al., 2015).
216 Observations and modelling of the dynamics and structure of Khumbu Glacier show that the lowest five
217 km (25% of the total length, 20% of total ice volume) is stagnant and dynamically detached from the
218 active glacier in the last century (Miles et al., 2021; Quincey et al., 2009; Rowan et al., 2021). Basal ice
219 at the glacier surface indicates that the active terminus overrides the stagnant glacier tongue (Miles et
220 al., 2021) and measurements of surface displacement show no longitudinal flow through the detached
221 debris-covered tongue, which is collapsing laterally at a rate of about 3 m a⁻¹ (Watson et al., 2017).

224 2.1 Glacier-climate model experimental design

225 As a starting point for our transient simulations of Khumbu Glacier, we reconstructed the late Holocene
226 glacier from an ice-free domain using an ELA of 5,325 m a.s.l. and an atmospheric lapse rate of 4.0°C
227 km⁻¹ in a 5 kyr simulation. The simulation continued through the LIA forced by forced by a step change
228 in mean annual air temperature (MAAT) equivalent to 1.5°C colder than the present day over 500 years
229 following Rowan et al. (2015, 2021). Ice-marginal moraines denoting the late Holocene (1.3 ± 0.1 ka)
230 glacier extent and thickness (Hornsey et al., 2022) were used to constrain the spin-up simulation. The
231 ice-free domain was found by subtracting the estimated ice thickness (Farinotti et al., 2019) from a 30-
232 m digital elevation model (DEM) acquired from the Shuttle Radar Topography Mission (Farr et al.,
233 2007). The ice-free model domain incorporated the full hydrological catchment including the steep
234 hillslopes in the Western Cwm that provide snow to the glacier surface by avalanching. We simulated

Deleted: sublimation and

Deleted: high-elevation

Deleted: The simulations

Deleted: because this is the period

Deleted: the

Deleted: and continue to 2300 CE using the best available projections of longer-term climate change.

Deleted: , but

Deleted: our

Deleted: through the subsequent two centuries

Deleted: surface energy and mass balance

Deleted: use

Formatted: Font colour: Auto

Formatted: Font colour: Auto

Formatted: Font colour: Auto

Formatted: Font colour: Auto

Deleted: at high elevations in

Deleted: monsoon-influenced Himalaya

Formatted: Font colour: Auto

Formatted: Font colour: Auto

Deleted: (Fig. 2).

Deleted: produces

Deleted: RCMs

Formatted: Font colour: Auto

Formatted: Font colour: Auto

Formatted: Font colour: Auto

Formatted: Font colour: Auto

Formatted: Font colour: Auto

Formatted: Font colour: Auto

Formatted: Font colour: Auto

Formatted: Font colour: Auto

Formatted: Font: Not Bold, Font colour: Auto

Formatted: Default, Add space between paragraphs of the same style

Moved (insertion) [2]

Moved (insertion) [3]

Moved (insertion) [4]

Moved (insertion) [5]

Moved (insertion) [6]

Moved (insertion) [7]

Deleted: and mass balance. We use RCMs to force the future climate scenarios and first evaluate their capabilities against observations of present-day weather and climate. In each simulation, we use

256 only the active section of the glacier to the present day and future, and assigned the detached debris-
257 covered tongue to the model domain as a static topographic feature. The late Holocene spin-up
258 simulation was forced to present-day conditions using three surface mass balances (one from each
259 RCM) calculated using the Coupled Snowpack and Ice-surface Energy and Mass Balance model in
260 Python (COSIPY v1.3) (Sauter et al., 2020). These simulations were evaluated against a range of
261 observations (Fig. 3) and the experiment using the NOAA RCM was identified as the starting point for
262 all future simulations because this was most representative of the observed glacier. For more detail on
263 the glacier model parameterisation and evaluation of the present-day simulation using geological and
264 remote sensing observations, we refer to Rowan et al. (2021).

266 The simulations continued from the present day to 2100 CE forced by the distributed glacier surface
267 mass balances calculated for each of the three RCMs and two RCPs using COSIPY. The three RCMs
268 and two future RCPs represent a range of possible future climates including distinctly different
269 precipitation trends, equivalent to dry, moderate and wet scenarios under warming of 1.4–2.2°C under
270 RCP4.5 and 3.8–4.1°C under RCP8.5 (Table 1; Section 2.2). We used climate time slices representing
271 the present day (2015–2020 CE) and the end of the 21st Century (2095–2100 CE) to calculate surface
272 mass balance. The five-year time slices were chosen to reduce the computational expense of the
273 modelling (~24 hours per simulation), and the preceding decade was used to evaluate these time slices,
274 Section 3.3). We used a step forcing rather than interpolating mass balance over time, whereby the
275 future mass balance was imposed and the glacier adjusted to this from the start of the century in
276 question. Thus we arrived at the present-day simulation from the LIA simulation by forcing the LIA
277 glacier with the 2015–2020 CE mass balance for 200 years. We use the output from the present-day
278 simulation with the 2095–2100 CE mass balance to force the model to 2100 CE for a period of 80 years.
279 We then use the result from this simulation as the starting point for the 2200 CE simulation forced by
280 the 2195–2200 CE mass balance for 100 years, and the same approach for the 2300 CE using the 2295–
281 2300 CE mass balance. Beyond 2100 CE, less detailed climate projections are available; given the
282 absence of regional climate projections, globally projected temperature changes were used to extend
283 the end-of-century mass balances. These gave a further increase in temperature of 0.5°C by 2200 CE
284 and 0.7°C by 2300 CE under RCP4.5, and 2.8°C by 2200 CE and 4.1°C by 2300 CE under RCP8.5
285 (Table 1; Collins et al., 2013). No precipitation changes were applied to the post-2100 CE climates due
286 to the absence of projections for precipitation in the CORDEX RCMs and the high uncertainties
287 associated with projections of global precipitation changes for this period.

289 We tested a range of lapse rates from 3.0°C km⁻¹ to 6.0°C km⁻¹ based on the range of monthly values
290 calculated from regression of NASA MODIS land surface temperature data for the Central Himalaya
291 while maintaining the same ELA, which resulted in a difference in ice volume of 0.4 x 10⁹ m³ and no
292 change in glacier length at the present day. We examined the uncertainty in accumulation resulting from
293 the application of a calculation to move snowfall from slopes susceptible to avalanching. Observations
294 of high-elevation Himalayan glaciers, including Khumbu Glacier, indicate that up to 75% of
295 accumulation occurs by avalanching rather than direct snowfall (Benn and Lehmkuhl, 2000).
296 Avalanching affects Khumbu Glacier in two ways: by moving snow from steep hillslopes onto the
297 glacier surface thus increasing accumulation from that calculated from direct snowfall onto the glacier
298 surface, and by redistributing snow across steep sections of the glacier surface. If avalanching was not
299 considered in the glacier model then accumulation of snow calculated using COSIPY within the
300 catchment but outside the glacier outline would have no impact on mass balance, resulting in an
301 underestimation of ice volume. When avalanching was not simulated, accumulation occurred at a
302 uniform rate of 2.0 w.e. m⁻¹ across the Western Cwm, and the resulting glacier had a similar extent
303 but a volume more than double that of the glacier simulated with avalanche redistribution of snow,
304 because mass was not redistributed effectively across steep sections of the glacier surface.

2.2 Present-day RCM downscaling using meteorological observations

306 Six RCMs were assessed on their fidelity to present-day climate, using hindcasting (Biemans et al.,
307 2013) with emphasis on temperature seasonality and seasonal precipitation dynamics, given the
308 importance of these variables for glacier mass balance. RCMs from the Coordinated Regional
309 Downscaling Experiment (CORDEX) South Asia domain, dynamically downscaled from CMIP5 GCMs
310

- Formatted: Font colour: Auto
- Deleted:)
- Formatted: Font colour: Auto
- Deleted: . The three RCMs and two future RCPs represent a range of possible future climates including distinctly different precipitation trends (Table 1) and are
- Formatted: Strong
- Deleted: as inputs to the glacier surface energy and
- Formatted: Strong
- Deleted: model COSIPY (Sauter et al. 2020). The resulting six mass balances (
- Formatted: Strong
- Deleted:
- Formatted: Strong
- Deleted: and future
- Formatted: Strong
- Deleted: each RCM force the glacier model (Rowan et al., 2015) from the late Holocene (~1 ka) through
- Formatted: Strong
- Deleted: day until 2100 CE, beyond which
- Formatted: Strong
- Deleted: only
- Deleted: . Given
- Formatted: Font colour: Auto
- Formatted: Font colour: Auto
- Deleted: beyond 2100 CE
- Formatted: Font colour: Auto
- Deleted: for RCP4.5 and RCP8.5, giving
- Deleted:
- Formatted: Font colour: Auto
- Formatted: Font colour: Auto
- Deleted:
- Deleted:
- Formatted: Font colour: Auto
- Formatted: Font colour: Auto
- Formatted: Font colour: Auto
- Deleted: high uncertainty in
- Formatted: Font colour: Auto
- Formatted: Font: Not Bold, Font colour: Auto
- Formatted: Default
- Moved (insertion) [8]
- Deleted: 2.1
- Deleted: , known as
- Deleted:),
- Deleted: that were

336 by the Indian Institute of Tropical Meteorology to a 50 km spatial resolution (Lutz et al., 2016) were
 337 downloaded for the grid box containing Khumbu Glacier (27.9065056°N, 86.4352951°E). Three of the
 338 six CORDEX South Asia RCMs (NOAA, CCCma, IPSL) spanning a range of possible future
 339 precipitation conditions (Table 1) were selected as discrete scenarios for the glacier surface energy and
 340 mass balance calculations. The three remaining RCMs were discounted due to being intermediate to
 341 those selected for our experiments (i.e. close to the future precipitation scenario represented by CCCma)
 342 or particularly poor at reproducing seasonal temperature and precipitation cycles. For example, despite
 343 the annual precipitation sums from the CSIRO RCM being closest to observed values and having the
 344 potential to be the ‘driest’ scenario examined, analysis of precipitation seasonality indicated that the
 345 monsoon signal was completely absent, with this RCM instead showing a strong dominance of winter
 346 precipitation.

347
 348 The present-day RCM results were downscaled using quantile mapping, also known as “distribution
 349 mapping”, using 14 years of observations from three automatic weather stations (AWS; Fig. 1c and
 350 Appendix A) collected between January 2006 and November 2019 with gaps filled using interpolated
 351 data from neighbouring stations if required (Fig. 2). Parametric quantile mapping (Piani et al., 2010)
 352 was used, whereby a statistical relationship between the raw climate model outputs and observations
 353 was formed by substituting the RCM results with observations at a cumulative density function of the
 354 prescribed distribution (e.g., a gaussian distribution for temperature; Luo et al., 2018; a gamma
 355 distribution for precipitation; Piani et al., 2010). This correction was applied to the raw RCM outputs
 356 to produce a third downscaled dataset with an improved fit to the observations (Maraun et al., 2016).
 357 The quantile mapping approach was chosen because this is effective for downscaling precipitation and
 358 reduces errors in the standard deviation, the coefficient of variation, and the skewness of distributed
 359 values relative to other methods (Lafon et al., 2013; Reiter et al., 2018). The AWS data were also used
 360 to disaggregate the resultant daily downscaled present-day and end-of-century climate model outputs
 361 to an hourly resolution for energy balance modelling. All meteorological variables, excluding
 362 precipitation, were downscaled using the MELODIST Python tool (Förster et al., 2016). Seasonal
 363 means were applied for precipitation to reproduce the ‘nocturnal peak’ seen during the monsoon that
 364 MELODIST was unable to replicate. Further information on RCM downscaling and AWS data analysis
 365 are provided in Appendix A.

366 2.3 Future RCM downscaling

367
 368 Two future emission scenarios (RCP4.5 and RCP8.5) were available from CORDEX South Asia, which
 369 represent only intermediate and high emissions by 2100 CE relative to the present day. These two
 370 emissions scenarios are frequently used in climate impact studies, enabling the comparison of our results
 371 with studies that use other climate/glacier model projections. The two future emissions scenarios were
 372 analysed for each of the three CORDEX RCMs to account for the inherently high uncertainties in future
 373 precipitation trends associated with climate models and the interplay of changing precipitation with
 374 atmospheric warming. The same statistical downscaling approach and disaggregation used for the three
 375 present-day RCMs (described in Section 2.2) was applied to the raw CORDEX RCM daily outputs for
 376 the three future RCM time slices under RCP4.5 and RCP8.5. The temperature change between the
 377 present day and the future time slices was preserved and there was no evidence of any imposed
 378 strengthening in the monsoon resulting from this downscaling. An increase in the frequency of days per
 379 year outside of the monsoon season with high precipitation amounts (defined here as over 15 mm of
 380 daily precipitation) accounted in large part for the higher annual precipitation amounts relative to the
 381 present day that were found in four out of the six RCMs. However, the total future annual precipitation
 382 increase was on average 8.8% greater in the downscaled climates relative to the raw RCMs, suggesting
 383 that this positive trend was inflated by downscaling. The downscaled climates reduced the frequency
 384 of precipitation, although, as in present day observations, monsoon precipitation occurred frequently
 385 and could be characterised as predominantly drizzle in the future.

386 2.4 COSIPY surface energy balance modelling

387
 388 COSIPY is a glacier surface energy and mass balance model that integrates a surface energy and mass
 389 balance model with a multi-layer snow and ice model (Weidemann et al., 2018; Sauter et al., 2020).
 390 COSIPY was chosen as it is currently considered a leading open-source method for estimating glacier

Deleted:) that has an elevation of about 2,100 m a.s.l.....
 Three of the six CORDEX South Asia RCMs (NOAA, CCCma, IPSL) that were observed to span...panning a range of possible future precipitation conditions (Table 1) were selected as discrete scenarios for the glacier surface energy and mass balance model experiments...alculations. The three remaining RCMs were discounted due to being intermediate to those selected for our experiments (i.e. close to the future precipitation scenario represented by CCCma) or particularly poor at reproducing seasonal temperature and precipitation cycles. For example, despite the annual precipitation sums from the CSIRO RCM being closest to observed values and having the potential to be the ‘driest’ scenario examined, analysis of precipitation seasonality indicated that the monsoon signal was completely absent, with this RCM (... [1])

Deleted: The NOAA RCM is characterised by the high (... [2])

Moved (insertion) [9]

Formatted: Font colour: Auto

Moved down [10]: and the West Changri Nup Glacier AWS

Moved down [11]: Where possible, precipitation data taken

Moved up [9]: Further information on RCM downscaling

Deleted: 14 years of meteorological observations were (... [3])

Deleted: 0.00554 °C m⁻¹ to adjust to the height of the (... [4])

Deleted: , particularly during high winds (Sherpa et al. (... [5])

Deleted: ¶ (... [6])

Deleted: are

Formatted: Font colour: Auto

Formatted: Font colour: Auto

Deleted: ,

Formatted: Font colour: Auto

Deleted: model or

Formatted: Font colour: Auto

Deleted: 1

Formatted: Font colour: Auto

Deleted: accounts

Formatted: (... [7])

Deleted: is

Formatted: (... [8])

Deleted: following

Formatted: Font colour: Auto

Deleted: occurs

Formatted: Font colour: Auto

Deleted: can

Deleted: into

Formatted: Font colour: Auto

Formatted: Font colour: Auto

Moved (insertion) [12]

Formatted: (... [9])

Formatted: Font colour: Auto

612 mass balance and has previously been applied to glaciers in High Mountain Asia. COSIPY includes a
613 calculation of sublimation, which is an important ablation process for high-elevation glaciers because
614 ablation can still occur if the latent heat flux is negative through sublimation, even in instances where
615 surface temperature and/or air temperature are well below the melting point (Bonekamp et al., 2021;
616 Brun et al., 2023; Huintjes et al., 2015). COSIPY integrates a surface energy balance model with a
617 multi-layer snow and ice model and thereby resolves all energy fluxes (F) at the ice surface that
618 contribute to surface melt (Q_{melt}):

$$F = SW_{in} \cdot (1 - \alpha) + LW_{in} + LW_{out} + Q_{sens} + Q_{lat} + Q_g + Q_{liq} \quad \text{Eq.(1)}$$

621
622 Where SW_{in} is incoming shortwave radiation, α is albedo, LW_{in} and LW_{out} are incoming and outgoing
623 longwave radiation, and Q_{sens} , Q_{lat} , and Q_g are the sensible, latent, and ground heat fluxes (Oerlemans
624 et al., 2001) and Q_{liq} is the heat flux from liquid precipitation; the latter variable is often neglected
625 in ablation calculations (Cuffey and Paterson, 2010) but is of particular importance here as the Indian
626 Summer Monsoon brings a significant amount of liquid precipitation to the lower reaches of Khumbu
627 Glacier. The resulting F is equal to the energy available for surface melt (Q_{melt}) when surface
628 temperature (T_s) is at melting point (0°C). T_s is used to calculate LW_{out} , Q_{sens} , Q_{lat} , Q_g and to partition
629 solid and liquid precipitation. When T_s exceeds the melting point it is reset to 0°C (273.15 K) and the
630 residual F fluxes equal Q_{melt} . In this instance, subsurface melt is triggered when the energy fluxes, for
631 example, penetrating SW_{in} warm the ice layer so that T_s exceeds the melting point of ice (Sauter et al.,
632 2020).

633
634 The COSIPY model domain was taken from the 30-m DEM that was resampled to 200-m grid spacing
635 following sensitivity analyses that revealed minimal impact on the results whilst greatly reducing
636 computational expense (Fig. 4). CORDEX RCM daily climate variables (temperature, precipitation, the
637 radiation components, wind speed, relative humidity and atmospheric pressure) were used to force
638 COSIPY. Snowfall measurements can be used as an input to COSIPY, but precipitation was partitioned
639 into rainfall and snowfall using the snow transfer scheme within COSIPY given the paucity of
640 observations and high uncertainties associated with AWS observations, climate reanalysis, and
641 modelled snowfall products for this region (Sauter et al., 2020). COSIPY was forced using hourly
642 meteorology with nine variables to calculate the energy balance and mass balance components at an
643 hourly time step from the sum of accumulation by solid precipitation, deposition, and refreezing of melt
644 water percolation, and ablation by melt and sublimation. The exchange processes at the surface,
645 including energy release and consumption with phase changes, control temperature distribution and
646 phase changes within the glacier (comprised of horizontal ice and snow layers). The coupling of the
647 surface energy balance component with a multi-layer subsurface snow and ice model accounts for
648 meltwater refreeze and percolation with the meltwater produced from the surface melt calculations
649 acting as an input. The mass balance was calculated at an hourly resolution, with accumulation resulting
650 from the accumulation of solid precipitation on the ice surface, refreeze of meltwater, and deposition
651 of water vapour, and ablation resulting from subsurface and surface melt and sublimation (Sauter et al.,
652 2020). The impacts of supraglacial debris on ablation and of snow avalanching on accumulation were
653 handled in the glacier model.

2.5 Glacier evolution modelling

654
655 The second-order shallow ice approximation model (iSOSIA) is a 3-D higher-order ice-dynamical
656 glacier evolution model that solves for the flow of ice including longitudinal and transverse stress
657 gradients that are imposed on ice flow through high-relief topography (Egholm et al., 2011). This glacier
658 model simulates the evolution of debris-covered glaciers by incorporating the feedbacks between debris
659 transport, mass balance and ice flow (Rowan et al., 2015) and includes two processes that are important
660 for many Himalayan glaciers—the redistribution of snow by avalanching that is estimated to account
661 for 75% of accumulation, and the formation of a supraglacial debris layer that insulates the ice surface
662 to modify ablation (Rowan et al., 2015). While previous versions of this glacier model used depth-
663 integrated ice flow, this version simulates the evolution of Khumbu Glacier in 3-D as the ice thickness
664 is divided into 20 vertical layers to calculate englacial debris transport (Rowan et al., 2015). The glacier
665

Moved (insertion) [14]

Moved (insertion) [15]

Formatted: Font colour: Auto

Formatted: Font colour: Auto

Deleted: 2.3 Surface energy and mass balance calculations

The Coupled Snowpack and Ice-surface Energy and Mass Balance model in Python (COSIPY) was used to calculate surface energy balance (Sauter et al., 2020). COSIPY is developed and modularised in Python and integrates a surface energy balance model with a multi-layer snow and ice model and thereby resolves all energy fluxes at the ice surface that contribute to surface melt.

Moved up [13]: COSIPY was chosen as it is currently considered a leading open-source method for estimating glacier mass balance and has previously been applied to glaciers in High Mountain Asia.

Moved up [16]: CORDEX RCM daily climate variables (temperature, precipitation, the radiation components, wind speed, relative humidity and atmospheric pressure) were used to force COSIPY. Snowfall measurements can be used as an input to COSIPY, but precipitation was partitioned into rainfall and snowfall using the snow transfer scheme within COSIPY given the paucity of observations and high uncertainties associated with AWS observations, climate reanalysis, and modelled snowfall products for this region (Sauter et al., 2020). COSIPY was forced using hourly meteorology with nine variables to calculate the energy balance and mass balance components at an hourly time step from the sum of accumulation by solid precipitation, deposition, and refreezing of melt water percolation, and ablation by melt and sublimation

Deleted: COSIPY includes a calculation of sublimation, which is an important ablation process for high-elevation glaciers (Bonekamp et al., 2021; Brun et al., 2023; Huintjes et al., 2015). The COSIPY model domain was taken from the 30-m digital elevation model (DEM) acquired from the Shuttle Radar Topography Mission (Farr et al., 2007) that was resampled to 100-m grid spacing following sensitivity analyses that revealed minimal impact on the results whilst greatly reducing computational expense.

Deleted: (Fig. 3). The impacts of supraglacial debris on ablation and the impacts of snow avalanching on accumulation were handled in the glacier evolution model. Further information on the use and evaluation of COSIPY is provided in Appendix B.

2.4

Deleted: While previous versions of this glacier model used depth-integrated ice flow, the version used here, and earlier studies, to simulate the evolution of Khumbu Glacier is fully 3-D as the ice thickness is divided into 20 vertical layers to allow for the calculation of englacial debris transport (Rowan et al., 2015). The glacier model has a variable time step that can adjust up to a maximum of 0.1 years to allow greater computational efficiency.

Deleted: glacier

Deleted: (Fig. 1d)

Deleted: .

720 model has a variable time step that can adjust up to a maximum of 0.1 years to allow greater
721 computational efficiency.

722
723 The distributed surface mass balances calculated using COSIPY using the downscaled RCMs for the
724 periods 2015–2020 CE and 2095–2100 CE were used as inputs to the glacier model with no change in
725 forcing applied between time steps. Surface processes within the glacier model modified the distribution
726 of accumulation and ablation but this was not updated into the surface topography used in COSIPY.
727 Simulated accumulation was the result of the total snowfall in each cell and avalanching of snow
728 imposed for the accumulated snowpack from hillslopes by removing snow and ice from hillslopes
729 greater than 28° and redistributing this mass across less steep surfaces using a non-linear hillslope flux
730 model (Roering et al., 1999). The avalanching routine was found to be sufficient to prevent snow and
731 ice accumulation on slopes that are observed to be free of glacier ice such as the southwest face of
732 Sagarmatha (Mt. Everest) while allowing accumulation on steep sections of the glacier (Rowan et al.,
733 2015), resulting in accumulation rates at the glacier surface in line with the limited available
734 observations for Himalayan glaciers of 2 m water equivalent (w.e.) per year (Benn and Lehmkuhl,
735 2000).

736
737 Rock avalanching is responsible for much of the debris accumulation on the glacier surface, but there is
738 little information about the magnitude and frequency of these events, so headwall erosion was assumed
739 to be uniform at 1 mm a⁻¹ (Rowan et al., 2021). Debris produced by headwall erosion was delivered to
740 the glacier surface using a similar non-linear hillslope flux model to snow avalanching. The reduction
741 in ablation beneath supraglacial debris from clean-ice values was represented as a reciprocal function
742 that scaled clean-ice ablation (b_{clean}) to give sub-debris melt (b_{debris}) as a function of debris thickness
743 (h):

$$744 \quad b_{debris} = b_{clean} \times \frac{h_0}{h + h_0} \quad \text{Eq. (2)}$$

745
746 where h_0 is a constant representing the characteristic debris thickness at which the reduction in ablation
747 due to insulation by supraglacial debris is 50% of the value for an equivalent clean-ice surface
748 (Anderson and Anderson, 2016; Rowan et al., 2021). The observed heterogeneity of surface ablation
749 required a parameterisation of sub-debris melt representing the effects of differential ablation, which
750 was represented in Equation (2) using a value for h_0 of 0.8 m (Bartlett et al., 2021; Rowan et al., 2021;
751 Strickland et al., 2023).

752 3. Results

753 3.1 COSIPY parameter perturbations

754 The sensitivity of glacier mass balance to individual meteorological variables (MAAT, radiative fluxes,
755 relative humidity, lapse rate, precipitation amount, precipitation phase, glacier surface roughness) was
756 calculated in experiments that perturbed these variables individually. Perturbations were made within
757 the range of the possible uncertainties for each variable that arise from a combination of the choice of
758 observations or climate models, the downscaling approach used, and the distribution of meteorological
759 variables. The values used for perturbations of MAAT and precipitation amount were similar to those
760 expected for possible future climate forcings.

761 The spatially averaged mass balance was most sensitive to changes in MAAT (perturbed by ±1.5°C,
762 2.0°C and 3.0°C), $LWin$ and $SWin$ (±10% and 20%). Perturbations of relative humidity (±10% and 20%)
763 had the least impact on mass balance. The use of a seasonal lapse rate of 5.38°C km⁻¹ yielded a spatially
764 averaged mass balance that was 5.6% less than the reference calculation value, while a diurnal lapse
765 rate gave a mass balance that was only 0.45% lower because the reference lapse rate was close to the
766 mean of the day/night lapse rates, whereas the environmental lapse rate (6.50°C km⁻¹) gave a mass
767 balance that was 1.24% higher than the reference value. The relatively small difference in mass balance
768 due to the choice of lapse rate is due to the extremely high elevation of Khumbu Glacier, which means
769 that MAAT is below 0°C in the accumulation area for much of the year and a higher lapse rate does not
770 affect rain/snow partitioning. The largest difference in mass balance due to the choice of lapse rate was

Deleted: and forced

Deleted: previously applied to Khumbu Glacier and

Deleted: whilst

Deleted: . The critical slope of 28° was selected because this threshold is low enough to prevent ice accumulation on slopes that are clearly ice-free today, but high enough to produce

Deleted: that are

Deleted: ,

Deleted: scales

Deleted: 1

Deleted: on the surface of Khumbu Glacier requires

Deleted: that represents

Deleted: is

Deleted: 1) by the

Deleted: chosen for h_0 that represents a positively skewed supraglacial debris thickness distribution including ablation 'hotspots' such as supraglacial ponds and ice cliffs, and is representative of the current state of Khumbu Glacier

Formatted: Justified

Moved up [4]: dynamically detached from the active glacier in the last century (Miles et al., 2021; Quincey et al., 2009; Rowan et al., 2021). Basal ice at the glacier surface indicates that the active terminus overrides the stagnant glacier tongue (Miles et al., 2021) and measurements of surface displacement show no longitudinal flow through the detached debris-covered tongue, which is collapsing laterally at a rate of about 3 m a⁻¹ (Watson et al., 2017).

Moved up [6]: estimated ice thickness (Farinotti et al., 2019) from

Moved up [7]: The ice-free model domain incorporated the full hydrological catchment including the steep hillslopes in the Western Cwm that provide snow to the glacier surface by avalanching. The

Deleted: 2.5 Glacier model experimental design

The late Holocene (~1 ka) glacier was reconstructed using a 5000-year equilibrium simulation starting from an ice-free domain and used as the starting point for three transient simulations through the 'Little Ice Age' maximum forced by a step change in mean annual air temperature (MAAT) equivalent to 1.5°C colder than the present day (Appendix B). The simulation was then forced to present-day conditions using the three surface mass balances (one for each RCM) calculated using COSIPY. The simulations continued to 2100 CE forced by the distributed surface mass balances calculated for each of the three RCMs and two RCPs using COSIPY. Khumbu Glacier is surrounded by ice-marginal moraines denoting the late Holocene (1.3 ± 0.1 ka) extent and ice thickness (Hornsey et al., 2022), which are used to constrain the spin-up simulation. Observations and modelling of the dynamics and structure of Khumbu Glacier show that (... [10])

Deleted: We therefore simulate only the active section of the glacier and assigned the detached debris-covered tong (... [11])

Deleted: the 30-m DEM.

Deleted: The late Holocene to present-day spin-up simulations of Khumbu Glacier were evaluated against (... [12])

864 of $\pm 24\%$ just below the ELA. The installation of the National Geographic automatic weather stations
865 on Mt. Everest in 2019 provided an opportunity to examine lapse rates at the highest elevations. For the
866 period April–November 2019, the observed lapse rate was $4.68^{\circ}\text{C km}^{-1}$ between Phortse (3,810 m a.s.l.)
867 and Everest Base Camp (5,315 m. a.s.l.) and $5.36^{\circ}\text{C km}^{-1}$ between Camp II and South Col, similar to
868 the value used in this study. The lapse rate above 8,000 m a.s.l. was about $1.2^{\circ}\text{C km}^{-1}$ greater than that
869 below 5,600 m a.s.l. between the two highest AWS (South Col and Balcony) indicating that in the
870 highest-elevation sections of the catchment, lapse rates may be best represented by values considered
871 suitable for the free atmosphere. The glacier ice surface roughness (z_0) value was 1.7 mm (Table 2),
872 which is a reasonable estimate for clean-ice glaciers (Mölg et al., 2012). The z_0 values reported in the
873 existing literature vary widely even for clean-ice glaciers and do not consider debris-covered glacier
874 surfaces, and so two substantially different z_0 values were tested as endmembers of the likely range in
875 z_0 values; 0.1 mm from Midtre Lovénbreen in Svalbard (Irvine-Fynn et al., 2014) and August-One
876 Glacier in China (Guo et al., 2018), and 6.9 mm for the clean-ice section of Haut Glacier D’Arolla
877 (Brock et al., 2006). Adjusting z_0 had minimal impact on mass balance, although a higher (lower) z_0 did
878 result in slightly increased (decreased) mass balance.

Moved (insertion) [18]

879
880 Coupled parameter testing involved perturbing precipitation and MAAT simultaneously. The most
881 significant change in spatially averaged mass balance followed a 3°C increase in MAAT and 20%
882 decrease in precipitation amount. The change in ablation following an increase in temperature of 1.5°C
883 was compensated by accumulation resulting from 20% higher precipitation. The impact on mass
884 balance of two precipitation phase (rain/snow) partitioning schemes was investigated and compared
885 with the default snow transfer function in COSIPY: (1) using threshold temperatures of 0.5°C , 2.0°C ,
886 and 3.5°C , and (2) using a calculation that smoothly scaled rain/snow partitioning from 100% solid
887 precipitation at -1°C to 0% solid precipitation at 4°C . The height of the 0°C isotherm during months
888 that experienced significant ablation (May–September) fluctuated around 5,125–6,250 m a.s.l., which
889 correlated with the elevations that experienced the greatest mass balance change with lapse rate. While
890 the lapse rate used to distribute MAAT did not have a significant impact on glacier-wide mass balance,
891 the elevation of the 0°C isotherm from the pre-monsoon until the end of the monsoon was sensitive to
892 the air temperature distribution.

893 3.2 Evaluation of COSIPY surface energy and mass balance results

894 Turbulent fluxes and energy balance components across Khumbu Glacier were explored across a three-
895 year period to assess the performance of COSIPY and understand their relative spatial importance. A
896 reference simulation was made using COSIPY for comparison with observed glacier mass balance and
897 tested across a range of grid spacings (30 m to 1 km). The reference simulation represented the period
898 2013–2015 CE and was forced by AWS data (Appendix A) using the model parameters in Table 2.

Deleted: the present-day climate

Deleted: glacier model

900
901 COSIPY was used to calculate clean-ice surface mass balance from the downscaled RCMs, and the
902 insulating effects of supraglacial debris were calculated in the glacier model. The glacier-wide clean-
903 ice mass balance for the three-year reference period was -3.4 m w.e, which equates to -1.13 m w.e a^{-1} .
904 Maximum ablation was up to 16.2 m w.e. over three years (Fig. 4). High precipitation events were
905 observed to offset some ablation if they occurred outside the core monsoon season (e.g., in October
906 2013 and May 2014) but did not influence monsoon season ablation when high air temperatures and
907 strong incoming radiative fluxes rapidly remove snow cover and drive melting. Higher minimum
908 temperatures in winter 2013–2014 CE relative to the other winters did not significantly influence
909 accumulation rates, which remained similar to those in 2014–2015 CE. Low precipitation amounts
910 during the 2015 monsoon (286 mm in 2015, compared to 330.8 mm in 2013, and 333.9 mm in 2014)
911 resulted in lower accumulation in the upper reaches of the glacier. The precipitation gradient was
912 calibrated to $1 \times 10^{-5} \% \text{ m}^{-1}$ to match observed accumulation rates. However, this gradient largely arises
913 from avalanching (Benn and Lehmkuhl, 2000) which is challenging to represent in COSIPY and was
914 instead handled in the glacier model (Section 2.5).

915
916 The energy available for ablation peaked in the pre-monsoon and monsoon, bringing higher rates of
917 sublimation and subsurface melt in April–June (Fig. 5). Simulated sublimation occurred at all
918 elevations, with the highest cumulative loss near the South Col (EB7910) where sublimation dominated

921 mass balance and only slightly slowed from December until May. Sublimation rates were increasingly
922 tied to seasonality with distance down-glacier, with rates on the lower section of the tongue (EB4980)
923 increasing from April until the start of the monsoon in July. Calculated subsurface melt was negligible
924 at or above the ELA (5,950 m a.s.l.) whereas at lower elevations sub-surface melt dominated mass
925 balance with a stronger seasonal cycle related to surface temperature. The interannual variability in
926 subsurface melt was linked to surface temperature, although low simulated subsurface melt rates in the
927 first year of the reference simulation were largely due to persistence of the initial snow cover that
928 shielded the subsurface from surface temperature until the subsurface adapted to local conditions.
929 Refreezing occurred across the entire glacier, with a staggered onset due to increased elevation, and the
930 absolute values were low. The higher latent heat flux during the monsoon resulted in higher deposition
931 of snow to the glacier at the lower elevations, with negligible rates at higher elevation. Similar absolute
932 values and patterns are seen for condensation.

933
934 Calculated incoming shortwave radiation matched well with observations from Ev-K2-CNR,
935 GlacioClim, and high-elevation AWS networks (Matthews et al., 2020) indicating that the radiation
936 model in COSIPY performed well across the extreme relief of the Khumbu Glacier catchment (Fig. 6).
937 Net shortwave radiation contributed the largest energy input to the glacier surface at lower elevations,
938 correlating most strongly with the energy available for melt with a mean correlation coefficient of 0.79.
939 There was high temporal variability related to variable cloud cover exhibited in the hourly incoming
940 shortwave radiation forcing and fluctuating albedo during the warmer months with the melting of the
941 snowpack. The high incoming shortwave radiation the upper reaches of the glacier indicate that low net
942 shortwave radiation is not due to topographic shading. Net shortwave radiation was correlated with
943 albedo ($r = 0.86$), and the persistence of snow throughout much of the year reduced the energy available
944 for melt. Net longwave radiation also contributed to the energy available for melt as the pattern of both
945 fluxes corresponded. ~~Between 5,900–7,900 m a.s.l., net longwave radiation sometimes exceeded zero~~
946 ~~during the monsoon, most likely due to heavy cloud cover and increased temperatures relative to the~~
947 ~~glacier surface. The latent heat flux was almost zero at the lower elevation sites as the arrival of the~~
948 ~~monsoon resulted in higher relative humidity, and this pattern was similar, but dampened, at higher~~
949 ~~elevation. At the South Col (EB7910) the energy available for melt correlated exactly ($r = 1$) with the~~
950 ~~sensible heat flux (Fig. 6).~~

951
952 Grid spacings for the climate-glacier model of 30 m, 50 m, 200 m and 1 km were tested to ensure that
953 that the COSIPY calculations captured orographic effects without unnecessary computational expense.
954 The simulated maximum accumulation rate did not change significantly with grid spacing, giving
955 accumulation rates of 2.1–3.9 m w.e. at 6,500–7,000 m a.s.l. in the reference simulation. The 1 km grid
956 spacing contained only 27 glacier points, and gave a similar spatial mean mass balance to the finer-
957 resolution calculations (Fig. 4), but there were large gaps in mass balance calculated across the glacier
958 that affected the height of the ELA and significantly reduced the calculated maximum accumulation
959 value. The 30-m and 50-m grid spacings captured greater spatial variability in mass balance relative to
960 the 200 m resolution calculation, particularly at elevations between 5200–5400 m a.s.l.. However, as
961 the ELA, and the calculated maximum and minimum mass balances were not significantly different
962 between these finer-resolution calculations, the 200 m grid spacing was used throughout to benefit from
963 the much reduced computational expense.

964 3.3 Evaluation of the RCM downscaling

965
966 The downscaled climate variables from the three RCMs for the present-day time slices (2015–2020 CE)
967 were evaluated against 14 years of observations from three AWS to assess the representation of means,
968 seasonality, diurnal cycles, day-to-day variability, and interannual variability. All three downscaled
969 RCMs showed good agreement between mean annual air temperature ($-2.15 \pm 0.05^\circ\text{C}$) and observed
970 air temperature from the Pyramid AWS (Appendix A). The representation of the monsoon was greatly
971 improved by the RCM downscaling; temperature seasonality was well resolved following quantile
972 mapping and the monthly mean and minimum air temperatures were similar to observations across the
973 present-day time slices (Fig. A1). The monsoon stabilised air temperatures and reduced the range
974 between minimum and maximum temperatures in the downscaled RCMs, which was in better
975 agreement with AWS observations, but was not present in the raw RCMs prior to downscaling. We note

Moved (insertion) [19]

Deleted: Each of the

Deleted: are

Deleted: show

Deleted: in their

Deleted: temperatures

Deleted: with

Deleted: temperatures

Deleted: is

Deleted: is

Deleted: are

Deleted: stabilises

Deleted: reduces

Deleted: is

Deleted: does

Deleted: occur

Deleted: .

992 that the downscaled maximum air temperature was at times higher than observations amongst all RCMs
 993 during the post-monsoon and winter (Fig. A1), but that the distribution of downscaled air temperatures
 994 was similar to observed values (Fig. A2). Gamma distribution quantile mapping substantially improved
 995 the absolute precipitation values relative to the AWS observations compared to those in the raw RCMs;
 996 the overestimation of winter precipitation and relative underestimation of monsoon precipitation
 997 amounts in the raw RCMs was reduced and downscaled results show a clearer monsoon signal (Fig.
 998 A3). When compared with AWS observations, RCM downscaling slightly over-corrected the seasonal
 999 precipitation pattern with a slight underestimation of winter precipitation for the most extreme winter
 1000 events. Across the three present-day simulations, the surface mass balance calculated using the NOAA
 1001 RCM was more positive than for the ISPL and CCCma RCMs and most similar to the mass balance
 1002 calculated from meteorological observations.

- Deleted: is
- Deleted: ,
- Deleted: is
- Deleted: improves
- Deleted: is
- Deleted: corrects
- Deleted: is

1004 3.4 Evaluation of the glacier model results

1005 The simulated glacier geometry and dynamics (Fig. 7) were compared with remotely sensed
 1006 observations of velocity, surface elevation change, and debris cover extent for the present-day glacier.
 1007 The distributed surface mass balances calculated using COSIPY were most similar to observed values
 1008 after the calculated surface mass balances were integrated with the glacier model to include
 1009 accumulation by snow avalanching and the reduction in surface melting beneath supraglacial debris;
 1010 the glacier extent was underestimated if supraglacial debris is not simulated (Fig. 8). The supraglacial
 1011 debris-mass balance feedback in the glacier model reproduced the observed reversed mass balance
 1012 gradient and peak in ablation below the Khumbu Icefall (Fig. 1). The simulated glacier area was 7.8
 1013 km² and similar to that obtained from structural mapping in 1979 CE (Nakawo, 1986). Radio-echo
 1014 sounding in 1999 CE obtained ice thickness estimates close to the active terminus of ~160 m (Gades et
 1015 al., 2000) and simulated ice thickness at the terminus was 130 m. The simulated thickness at the active
 1016 glacier terminus thickness was approximately 175 m in 1999 CE, which agreed well with observations
 1017 from DEMs of difference that show thinning here of up to 55 m between 1984–2018 CE (King et al.,
 1018 2020). Simulated surface elevation change in the ablation area was –30 m over 20 years to the present
 1019 day and similar to values derived from satellite observations for 1984–2015 CE (King et al., 2020).
 1020 Simulated present-day glacier velocities (Fig. 9) show a similar pattern and magnitude to glacier surface
 1021 velocities observed using remote sensing observations, which reach a maximum of 220 m a⁻¹ in the
 1022 Khumbu Icefall (Altena and Kääh, 2020) and up to 20 m a⁻¹ in the ablation area (Quincey et al., 2009;
 1023 Dehecq et al. 2019). The simulated present-day velocities in this study were a better fit to remote sensing
 1024 observations than those from previous simulations that used an elevation-dependent mass balance
 1025 forcing (Rowan et al., 2015, 2021) where the maximum simulated velocities were 118 m a⁻¹.

- Deleted: 4) are
- Deleted: and moraine positions indicating the extent during the late Holocene (~1 ka) and Little Ice Age (~500 a) maxima (Hornsey et al., 2022) are compared to the equivalent periods in the simulation (Appendix B). The distributed surface mass balances calculated using COSIPY are most similar to observed values after the calculated surface mass balances are
- Deleted: is underestimated if supraglacial debris is not simulated (Fig. 5). The supraglacial debris-mass balance feedback in the glacier model reproduces the observed reversed mass balance gradient and peak in ablation below the Khumbu Icefall (Fig. 1) (Benn and Lehmkuhl, 2000; King et al., 2020). The simulated glacier area was 7.8 km²—
- Deleted: is
- Deleted: agrees
- Deleted: is
- Deleted: 6
- Deleted: that
- Deleted: are

1027 3.5 Climate change and glacier evolution from the present day until 2100 CE

1028 Khumbu Glacier is responding to historical climate change and will continue to shrink even if warming
 1029 ceases today. Indeed, if we allow the spin-up experiment to reach equilibrium with the present-day
 1030 NOAA RCM mass balance, the glacier terminus will recede by 2.1 km and the maximum ice thickness
 1031 will decrease from 246 m to 206 m by 2100 CE without any additional warming (Fig. 10a). In this
 1032 simulation, a supraglacial debris layer up to 1.3 m thick extends 1 km up-glacier from the terminus and
 1033 partially dampens the committed volume loss by sustaining 13% more ice volume than would be the
 1034 possible for a clean-ice glacier surface with the same mass balance. The committed glacier volume loss
 1035 due to historical warming in the absence of any further climate forcing is 10–23% of the present-day
 1036 glacier mass (Fig. 9b) with the associated uncertainty represented by this range of values arising from
 1037 the parameterisation of the impact of supraglacial debris evolution on surface melting.

- Deleted: 2
- Deleted: 7a
- Deleted: volume
- Deleted: 7b

1039 Now considering the effects of additional warming under the RCP scenarios for the NOAA experiment,
 1040 we find that greater warming occurs in winter than in summer under both RCPs (Sanjay et al., 2017)
 1041 and results in an increase in annual precipitation amount of about 15% made up of a greater increase in
 1042 winter precipitation than summer precipitation. The climate forcing from the downscaled NOAA RCM
 1043 under RCP4.5 is 1.4°C warmer than the present day (–0.75°C in 2095–2100 CE compared with –2.15°C
 1044 in 2015–2020 CE) and annual precipitation increases by 14.8% from 581.4 mm at present day to 664.8
 1045 mm a⁻¹ by 2100 CE with summer (June–September) precipitation increasing by 5.4% and winter
 1046 (December–February) precipitation increasing by 14.1% (Fig. 2). Under RCP8.5, the downscaled

- Deleted: Greater
- Deleted: %,

1079 climate forcing is projected to be 3.8°C warmer than present day (1.65°C in 2095–2100 CE) with an
1080 increase in annual precipitation of 14.9% by 2100 CE, with summer precipitation increasing by 9.8%
1081 and winter precipitation increasing by 19.4%. In the NOAA RCM RCP4.5 experiment, the spatially
1082 averaged cumulative glacier mass balance is $-0.14 \text{ m w.e. a}^{-1}$ in 2100 CE, which is slightly more
1083 positive than the present-day value of $-0.21 \text{ m w.e. a}^{-1}$. Glacier volume decreases by 36% between the
1084 present day and 2100 CE (Fig. 10). While significant, this end-of-century glacier loss is partially offset
1085 by the concurrent increase in precipitation. In comparison, an equivalent simulation forced only by
1086 warming and without any change in precipitation results in a more linear trajectory of glacier change
1087 and 70% loss of glacier volume by 2100 CE (light blue line in Fig. 10d) demonstrating that 34% of
1088 potential glacier loss from warming could be compensated by the increase in precipitation that occurs
1089 as a result of warming.

1090
1091 The CCCma and IPSL RCMs projected greater warming from the present day by 2100 CE than the
1092 NOAA RCM under RCP4.5 with a value of 1.6°C (+0.2°C compared with the NOAA RCM) in the IPSL
1093 RCM experiment and 2.2°C (+0.8°C) in the CCCma RCM experiment. These two RCMs also projected
1094 slightly greater warming by 2100 CE under RCP8.5, with a value of 3.9°C (+0.1°C compared with the
1095 NOAA RCM) for the IPSL RCM experiment and 4.1°C (+0.3°C) for the CCCma RCM experiment. The
1096 projected increase in precipitation amount across the three RCMs is similar between RCPs with annual
1097 totals above 600 mm by 2100 CE. The CCCma RCM gives the greatest increase in annual precipitation
1098 amount of 100 mm by 2100 CE. There is no evidence of change in the intensity of the Indian Summer
1099 Monsoon, as the seasonal split in precipitation remains similar to the present day, but the frequency of
1100 days with high precipitation (over 15 mm per day) increases by 2100 CE, giving twice as many days in
1101 the NOAA RCM experiment and up to seven times as many days in the IPSL RCM experiment. Under
1102 RCP8.5, all experiments showed similar results for mass balance by 2100 CE with only a 10%
1103 difference in glacier volume between the three RCMs (Fig. 10d). The CCCma RCM experiment has
1104 only a 1% difference in volume loss between RCP4.5 and RCP8.5 by 2100 CE despite a 1.9°C
1105 difference in MAAT—this is a surprising result given the significant temperature difference, which can
1106 be attributed to the greater number of high-magnitude precipitation events that occur under RCP8.5 in
1107 combination with the small difference in winter temperatures between the two RCPs. Indeed, in the
1108 CCCma RCM experiment under RCP4.5, the maximum winter temperature is 1.7°C higher than for the
1109 other RCMs, resulting in ablation and rainfall (rather than snowfall) during the winter.

1110 3.6 Climate change and glacier evolution from 2100 CE until 2300 CE

1111 Projections of climate change beyond 2100 CE are more uncertain than those for this century and the
1112 uncertainties associated with the model experimental design become larger, but these results do indicate
1113 a future trajectory for Khumbu Glacier. As there are no regional temperature projections beyond 2100
1114 CE we used global values to continue the simulations into the next century (Table 1). However, there
1115 are no global projections of precipitation beyond 2100 CE and to avoid introducing potentially
1116 significant uncertainties to our results by estimating these values, no changes in precipitation were
1117 applied beyond 2100 CE.

1118
1119 In all the RCP4.5 experiments, there is little change in glacier volume between 2200 CE and 2300 CE
1120 compared with 2100 CE regardless of the RCM forcing used (Table 1 and Fig. 10b). In the NOAA
1121 RCP4.5 experiment, the Khumbu Icefall is maintained until 2300 CE and ice continues to flow from
1122 the Western Cwm to below 6,000 m so that the glacier remains in contact with the dynamically detached
1123 tongue. Therefore, keeping warming within the limit of RCP4.5 could restrict future volume loss to
1124 only 26% beyond that already committed to by historical climate change, and Khumbu Glacier would
1125 reach a new dynamic equilibrium that maintains a sufficient ice thickness to survive for at least two
1126 centuries. However, in all the RCP8.5 experiments, substantial glacier loss occurs after 2100 CE and
1127 Khumbu Glacier completely decays before 2300 CE.

1128
1129 Physical detachment of the debris-covered tongue from the active glacier, whereby this area contained
1130 no active glacier ice, occurs around 2140 CE in the NOAA experiment (Fig. 9) and around 2070 CE in
1131 the CCCma and IPSL experiments. We defined the glacier to be stagnant when the maximum rate of
1132 ice flow is less than 10 m a^{-1} ; a conservative estimate of the uncertainty associated with observations
1133

Deleted: The

Deleted: In the NOAA RCM RCP4.5 experiment, glacier

Deleted: decreased

Deleted: 7

Deleted: the

Deleted: 8

Deleted: project

Deleted: project

Deleted: show

Deleted: 7

Deleted: 3

Deleted: give rise to

Deleted: clear prognosis

Deleted: use

Deleted: There

Deleted: are

Deleted: 7b

Deleted: will

Deleted: ¶

In...

Deleted: contains

Deleted:) (Fig. 6).

Deleted: define

1158 of glacier velocities (Dehecq et al., 2019). Accordingly, we consider Khumbu Glacier to no longer be a
1159 viable glacier system at the point where there is no ice flow above this value in the entire glacier since
1160 there is minimal throughput of ice mass. In the NOAA RCP8.5 experiment, the glacier area is 1.2 km²
1161 and the mean velocity reduces to 10 m a⁻¹ by 2260 CE, such that the glacier is no longer viable. Glacier
1162 breakdown occurs earlier for the CCCma and IPSL RCM experiments (Fig. 10b) by 2170–2180 CE
1163 because loss of ice volume due to warming is not compensated to the same magnitude by the increase
1164 in precipitation projected under RCP8.5 in the NOAA RCM experiment.

Deleted: as an active system.

1166 4. Discussion

1167 4.1 Uncertainties associated with the climate-glacier modelling approach

1168 Sources of uncertainty in our results arose from each step of our climate-glacier modelling workflow,
1169 and we considered how the experiments could be designed to reduce these uncertainties. In this section
1170 we discuss the potential sources of uncertainty associated with the choice of RCMs, the downscaling
1171 of the RCMs, the use of time slices rather than continuous mass balance calculations, the representation
1172 of future precipitation in the RCMs, the use of GCM forcing beyond 2100 CE, and the representation
1173 of avalanching in the glacier model.

Deleted: The climate-mass balance forcing ensemble was limited in size due to the small number of RCMs available for the CORDEX South Asia region and in this study we considered all of the relevant available forcings.

1175 A single RCM was not considered sufficient to represent both present-day climate and potential future
1176 climatic extremes, but the climate-mass balance forcing ensemble was limited in size due to the small
1177 number of RCMs available. The use of three RCMs allowed the implications of uncertainties in
1178 understanding of local climate for glacier evolution to be evaluated. A multi-model mean approach
1179 using all the CORDEX South Asia RCMs (widely used elsewhere) was not considered sufficient to
1180 represent present-day and future climate conditions in the Khumbu Valley, as this approach gives equal
1181 weighting to models irrespective of their performance (Pierce et al., 2009) and does not enable
1182 intercomparison of results for future climate conditions. Five-year downscaled RCM time slices were
1183 chosen to reduce computational expense associated with COSIPY and the integration with the glacier
1184 model. To ensure that the five-year periods selected were representative, the preceding decade was used
1185 for comparison with the time-slice results (Appendix A). The use of quantile mapping with 14 years of
1186 AWS data as the downscaling method limited the influence of any natural variability by ensuring that
1187 the period did not reflect an extreme phase of natural climate oscillation. This comparison was
1188 particularly important for the future time slices, where large uncertainties arise between RCMs and
1189 observational data cannot be used for evaluation of the downscaled climate or the resulting mass
1190 balance.

Deleted: but the

Deleted: ,

Deleted: ,

1192 The time slice approach resulted in a stepped response in terms of ice volume change over time where
1193 the forcing was changed (Fig. 10d). The glacier continued to evolve through each century rather than
1194 equilibrate with the mass balance forcing, but we note that this stepped approach could be improved by
1195 interpolating the mass balance over time and coupling the COSIPY and iSOSIA models such that mass
1196 balance was calculated dynamically for the evolving ice surface; however this was beyond the scope of
1197 our experiments. The experiments were repeated using mid-century (2045–2050 CE) mass balance
1198 forcings to simulate glacier evolution until 2100 CE to investigate if this produced a different end-of-
1199 century result. These experiments produced near-identical results in 2100 CE to the experiments with
1200 no mid-century forcing, because the response time of the simulated glaciers was longer than the 40-
1201 year period between the present-day and future time slices. Thus, a mid-century surface mass balance
1202 forcing was not considered necessary in our experiments and instead we used a step forcing for mass
1203 balance rather than interpolation between mass balance calculations in the glacier model. The
1204 reacceleration in glacier mass loss after 2100 CE was in part due to the stepped forcing approach and
1205 the uncertainties associated with GCM projections, which increase with time after 2100 CE particularly
1206 under RCP8.5. For example, forecasts of global warming for 2281–2300 CE relative to 1986–2005 CE
1207 under RCP8.5 range from 3.0°C to 12.6°C (Collins et al., 2013).

Moved (insertion) [20]

1209 The differences in simulated glacier change and response time that resulted from the RCMs were at
1210 times greater than those resulting from the RCPs due to differences in projections of precipitation.
1211 Whilst the three selected RCMs performed relatively well in representing annual precipitation cycles
1212 from the six available CORDEX RCMs, we note that this representation was still fairly poor, although

Formatted: Font colour: Auto

Formatted: Default

1221 substantially improved by quantile mapping. The poor representation of monsoon dynamics in the
 1222 present-day RCMs highlights an additional uncertainty associated with future precipitation scenarios
 1223 and that these results should be treated as a set of possible scenarios. The CORDEX CMIP5 and CMIP6
 1224 projects only produced dynamically downscaled RCMs for two future emissions scenarios (RCP4.5 and
 1225 RCP8.5) and as such the implications of other RCPs for glacier evolution could not be assessed. The
 1226 downscaled future climates were compared with those from other studies using CORDEX results, and
 1227 showed similar annual and seasonal regional temperature trends strongly linked to the choice of RCP,
 1228 and similar positive precipitation trends with poor agreement between RCMs (Kaini et al., 2019; Sanjay
 1229 et al., 2017). The relationship between precipitation and **warming in** the two future emissions scenarios
 1230 was less clear than that for air temperatures, because the monsoon-influenced Himalaya **has** particularly
 1231 poor RCM consensus and high levels of uncertainty in future precipitation trends with warming relative
 1232 to other regions in High Mountain Asia (Sanjay et al., 2017). **The transition in the glacier model between**
 1233 **the downscaled RCM and the GCM forcing could be improved by homogenising the climate model**
 1234 **results across 2090–2100 CE, however, as noted above, the computational expense of forcing COSIPY**
 1235 **with downscaled RCM outputs to create inputs to the glacier model, required the use of a time-slice**
 1236 **approach that was limited to five-year periods, and integration of the RCM results with GCM results**
 1237 **was beyond the scope of this study.** In the absence of RCMs that can project changes in precipitation
 1238 after 2100 CE, precipitation was maintained at the same level for the glacier surface energy and mass
 1239 balance model simulations beyond 2100 CE. The end-of-century precipitation amount is **therefore**
 1240 unlikely to be reflective of the more distant future, and more realistic precipitation projections are
 1241 required to explore whether the active glacier can be sustained further into the future or will lose ice
 1242 more rapidly than is found in this study. However, while future precipitation changes may be important
 1243 for glacier volume change under RCP4.5, we do not expect a sufficient increase in precipitation beyond
 1244 2100 CE to compensate for the warming projected under RCP8.5.

1245 **A large uncertainty in the glacier model arose from the parameterisation of avalanching, which** resulted
 1246 in increased accumulation along the glacier surface in the Western Cwm and improved the agreement
 1247 between simulated and observed accumulation rates and distribution, (Benn and Lehmkühl, 2000).
 1248 Future work to resolve the impact of low frequency–high magnitude avalanche events on accumulation
 1249 rates would **be useful** to refine this calculation but the contribution of avalanches to glacier
 1250 accumulation over decadal time scales remains challenging to measure. Our study addresses fine-scale
 1251 temporal (hourly) and spatial (100 m) glacier surface processes, including avalanching and sublimation,
 1252 that affect glacier surface mass balance across the elevation range of Khumbu Glacier, but further
 1253 observations of meteorological and glaciological conditions at the highest elevations would be
 1254 beneficial, and are needed if micro-scale processes are to be included in glacier models (Brun et al.,
 1255 2023; Khadka et al., 2021; Mölg et al., 2014; Shaw et al., 2022).

1257 4.2 Comparison with outcomes under RCP8.5

1258 Current global greenhouse gas emissions are following the trajectory of the intermediate emissions
 1259 scenario RCP4.5, while the high emissions scenario RCP8.5 could be described as ‘low possibility but
 1260 high impact’ (Pedersen et al., 2020). However, **as represented in the RCMs used in our study,** mountain
 1261 regions are warming more rapidly than the global mean such that a global temperature rise of 1.5°C will
 1262 lead to $2.1 \pm 0.1^\circ\text{C}$ of warming in High Mountain Asia (Kraaijenbrink et al., 2017; Pepin et al., 2022)
 1263 although the occurrence of elevation-dependent warming above 5,000 m a.s.l. is debated (Gao et al.,
 1264 2018). **The high temperatures projected under RCP8.5 could potentially be offset partly by increased**
 1265 **precipitation, given that high-magnitude precipitation events from winter Westerly disturbances**
 1266 **increased by a factor of seven between present day and 2100 CE in the IPSL RCM under RCP8.5.**
 1267 However, we found no evidence of future increases in precipitation offsetting RCP8.5 warming; net
 1268 glacier mass balance was strongly negative in all RCP8.5 experiments and insufficient to maintain any
 1269 actively flowing glacier. Under RCP8.5, glacier mass balance in the monsoon-influenced Himalaya may
 1270 therefore shift from being driven by accumulation during the monsoon to predominantly during winter.
 1271 Monsoon precipitation would only result in snow accumulation at the very highest elevations and would
 1272 be insufficient to maintain flowing glaciers. This outcome is avoidable by limiting anthropogenic
 1273 warming to within RCP4.5, which, due to the associated increase in precipitation, could sustain nearly
 1274

Formatted: Font colour: Auto

Deleted: ,

Formatted: Font colour: Auto

Deleted: shows

Formatted: Font colour: Auto

Deleted: ¶

¶ Five-year

Deleted: time slices were chosen to reduce

Deleted: associated with

Deleted: and the integration

Deleted: . To ensure

Deleted: the

Deleted: selected were representative, the preceding decade was used for comparison with the time-slice results, although the use of quantile mapping with 14 years of reference AWS data as the downscaling method will limit the influence of any natural variability by ensuring that

Deleted: period is not reflecting an extreme phase

Moved up [20]: For example, forecasts of global warming for 2281–2300 CE relative to 1986–2005 CE under RCP8.5 range from 3.0°C to 12.6°C (Collins et al., 2013).

Deleted: natural climate oscillation. This comparison was particularly important for the future time slices where large uncertainties arise between RCMs and there are no observations for evaluation of the downscaled climate or surface mass balance. An experiment was conducted using mid-century (2045–2050 CE) mass balance forcings to investigate any effect on glacier-climate imbalance. This experiment produced near-identical results in 2100 CE to the experiments with no mid-century forcing, because the response time of the simulated glaciers was longer than the 40-year period between the present-day and future time slices, and so the mid-century surface mass balance forcing was not considered necessary in our experiments. ¶

¶ The uncertainties associated with GCM projections increase with time after 2100 CE, particularly under RCP8.5.

Deleted: ,

Deleted: therefore

Formatted: Font colour: Auto

Deleted: The

Deleted: in the glacier model

Deleted: .

Deleted: help

Deleted: of

Deleted: RCP4.5 and

Deleted: High

Deleted: the

Deleted: , and could result in net annual glacier mass balances that are less negative than would be the case when solely forced by warming

1323 two thirds of the current glacier volume until 2100 CE and potentially for two centuries further into the
1324 future.

1325
1326 A recent global glacier modelling study forced by an ensemble of 10 GCMs projected mass loss of 64%
1327 for Khumbu Glacier by 2100 CE (Rounce et al., 2023). In comparison, our experiments project less
1328 severe rates of decline, resulting in 30% less mass loss under the RCP4.5 future climate scenario than
1329 in the global study (Fig. 10d). One difference between these results is that rather than using the global
1330 glacier inventory outline to define the glacier margins we consider only the actively flowing glacier and
1331 so exclude 20% of the starting glacier volume in the detached tongue. We would expect the two sections
1332 of the glacier to evolve along different paths; while the active glacier responds to climate change as
1333 projected in our experiments, thick supraglacial debris mantling the detached tongue could allow this
1334 ice mass to survive and slowly decay *in situ* for many decades beyond the present day. The decay of the
1335 detached tongue may however increase due to erosion of the surface by ice cliffs and supraglacial water
1336 bodies that are expanding across the former glacier surface (King et al., 2020). Our experiments only
1337 consider the rapidly changing active glacier, and we expect that the debris-covered tongue would melt
1338 more slowly than projected in the global modelling study, but as we do not consider the stagnant tongue
1339 to be part of the present-day glacier the ice volume simulated at the start of our experiments is smaller
1340 than that represented by Rounce et al. (2023) and other studies based on the RGI glacier inventory. The
1341 dynamically detached debris-covered tongue represents 20% of the present-day glacier volume and
1342 contains ice estimated as up to 360 m thick. The mean present-day ablation rate across this section of
1343 the glacier simulated in Rowan et al. (2021) is $-0.54 \text{ m w.e. a}^{-1}$ which can be used to estimate the life
1344 expectancy of the debris-covered tongue assuming no input of ice from the active glacier and no change in
1345 ablation rate due to thickening of supraglacial debris or the development of ice cliffs and supraglacial
1346 ponds. While the thickest part of the detached tongue may survive for ~ 600 years, the mean life
1347 expectancy of this ice mass is 176 ± 148 years from the present day meaning that the former debris-
1348 covered tongue will vanish by 2200 CE.
1349

1350 4.3 Impacts of microscale meteorology on glacier change

1351 Sublimation simulated in our study occurred at all elevations with the highest rate of ice loss due to
1352 sublimation ($-0.12 \text{ m w.e. a}^{-1}$) in the upper reaches of the Khumbu Glacier catchment near to South Col
1353 (about 7,495 m a.s.l.) where sublimation dominated ablation with only minor seasonality. Whilst this
1354 amount of ice loss by sublimation is not negligible, it is almost half that found in the point-based
1355 calculations after adjusting for the different time periods represented by our studies (Matthews et al.,
1356 2020), which is likely due to the assumed uniformity of wind speed across the model domain in
1357 COSIPY. Future work to improve the calculation of sublimation in distributed surface mass balance
1358 calculations for high-elevation glaciers would be valuable. While we have considered the effects of
1359 mesoscale meteorology on glacier mass balance, smaller-scale processes operating close to the land
1360 surface could also be important. Katabatic winds were suggested to explain a local 15-year decrease in
1361 maximum air temperatures and precipitation over glaciers while minimum air temperatures continued
1362 to rise (Salerno et al., 2023). However, the impact of micro-scale near-surface cooling on the duration
1363 and extent of mesoscale precipitation and accumulation is likely to be minimal and therefore unlikely
1364 to significantly affect glacier-wide mass balance (Mott et al., 2020; Shaw et al., 2024). Observations
1365 from an AWS on Khumbu Glacier (6,464 m a.s.l.) indicate that surface energy fluxes may be sufficient
1366 to cause non-negligible melting of glacier surfaces despite freezing air temperatures (Matthews et al.,
1367 2020). Results from an ice core from South Col Glacier ($>8,000 \text{ m a.s.l.}$) combined with COSIPY
1368 experiments suggested that ablation may also take place at even at the highest elevations (Potocki et al.,
1369 2022). However, a subsequent study found no evidence of change, and identified large uncertainties
1370 associated with simulating mass balance at these extreme elevations where sub-daily air temperature
1371 gradients and the duration of snow cover strongly affect ablation and accumulation (Brun et al., 2023).
1372 Future work is needed to reduce these uncertainties, as very few observations of accumulation processes
1373 and the upper limit of ablation processes exist for high-elevation Himalayan glaciers.
1374

1375 4.4 The response of large debris-covered glaciers to climate change

1376 The dynamic response time of large glaciers to climate change is of the order of centuries; for this
1377 reason, we start our simulations from the late Holocene ($\sim 1 \text{ ka}$) moraine extent when Khumbu Glacier

Deleted: Comparing our results to those for the same

Deleted: from a global

Deleted: showed that

Deleted: ice volume

Deleted: a smaller amount of loss by 2100 CE (Fig. 8). In our experiments, there is 39

Deleted: and 32% less under RCP8.5

Deleted: .

Deleted: .

Deleted: .

Deleted: of

Deleted: around

Deleted: dominates

1391 was last considered dynamically stable (Hornsey et al., 2022; Rowan et al., 2015). The relationship
1392 between glacier response time and mass balance becomes less important after 2100 CE when the glacier
1393 is so small that ice flow has little impact on glacier volume change. Global and regional glacier
1394 modelling studies typically start their simulations in the current century (e.g., 2000–2007 CE in
1395 Marzeion et al. (2020); 2015 CE in Rounce et al. (2023)) and a further complication arises from the use
1396 of global glacier inventories as a starting point for glacier modelling studies as such inventories cannot
1397 capture the current dynamic state of glaciers that are imbalanced, and include all ice-covered areas
1398 rather than identifying only actively flowing ice. However, satellite-derived velocity products could be
1399 used to identify where ice flow within glacier outlines declines to negligible rates (Dehecq et al., 2019).

1400
1401 The RGI 7.0 inventory for Khumbu Glacier is based on imagery from 1999 CE (RGI 7.0 Consortium,
1402 2023) where the detached debris-covered tongue represents 20% of the glacier volume contained within
1403 this outline (Fig. 1c). Simulations that integrated the stagnant tongue into the model domain rather than
1404 as part of the flowing ice improved the representation of simulated ice flow compared to observed
1405 values, supporting our conclusion that the debris-covered tongue has been dynamically detached from
1406 the active glacier for 50–100 years (Rowan et al., 2021). Field observations support the concept of
1407 active and stagnant sections co-existing in contact with each other as englacial optical televiewing
1408 indicated that thrusting occurs at several sites, denoted by skewed internal debris layers and of basal ice
1409 that has been thrust to the glacier surface, near to the active glacier terminus (Fig. 1c) from the direction
1410 of Khumbu Icefall (Miles et al., 2021). Our simulations show that development of supraglacial debris
1411 at the active glacier terminus reduced net volume loss by 13% (Fig. 8). Dynamic detachment of debris-
1412 covered tongues could allow these glaciers to move closer to equilibrium with a rapidly changing
1413 climate, the local mass balance gradient is a more important control on glacier change for both clean-
1414 ice glaciers and debris-covered Himalayan glaciers.

1415 5. Conclusions

1416 In the monsoon-influenced Himalaya, 85% of the glacier area is located higher than 5,000 m above sea
1417 level and 21% is above 6000 m. Despite these high elevations, Himalayan glaciers are rapidly losing
1418 ice in response to recent warming and are projected to shrink by 53% to 70% during this century.
1419 However, the impact of future changes in precipitation on glacier loss remains uncertain, because
1420 mesoscale meteorology is not often represented in glacier model projections. We explored the effects
1421 of future warming in tandem with changes in precipitation by simulating the evolution of Khumbu
1422 Glacier in the Everest region of Nepal—a benchmark glacier in the monsoon-influenced Nepal
1423 Himalaya—using mesoscale glacier surface energy and mass balance modelling forced by downscaled
1424 Regional Climate Model outputs. Historical warming commits Khumbu Glacier to loss of 10–23% of
1425 the total ice volume by 2100 CE. While warming due to intermediate future greenhouse gas emissions
1426 (RCP4.5) will lead to glacier volume loss of 70% by 2100 CE, the projected concurrent increase in
1427 precipitation amount will offset 34% of this and so reduce glacier loss by about a half. However, high
1428 future emissions (RCP8.5) will not be compensated by changes in precipitation amount but will instead
1429 result in substantial ablation above 6,000 m with devastating consequences for one of the highest
1430 glaciers on Earth. Our results indicate that the net mass balance of Khumbu Glacier could be close to
1431 zero in 2100 CE under RCP4.5 and therefore, if climate change is limited to this intermediate emissions
1432 scenario, Khumbu Glacier will recede to the base of the icefall with insignificant further change in
1433 glacier volume beyond this point. In this scenario, Khumbu Glacier has a similar extent in 2100 CE to
1434 the active section of the present-day glacier, and represents at least one example of how monsoon-
1435 influenced Himalayan glaciers could persist into the future if global efforts are sufficient to mitigate
1436 anthropogenic climate change.

1437
1438
1439
1440

Deleted: (

Deleted: .,

Deleted: (

Deleted: .,

Deleted: ,

Deleted: 5) but that otherwise the glacier surface is clean (Fig. 4). Therefore, while supraglacial debris sustains about 13% of additional glacier volume compared to a clean-ice surface, after dynamic

Deleted: above

Deleted: and cause Khumbu Glacier to vanish by 2160–2260 CE....

1453 **Code availability**
1454 The COSIPY [version 1.3](#) glacier surface energy and mass balance model is available from the original
1455 publication describing this model (Sauter et al., 2020) and [Zenodo \(Arndt et al., 2020\)](#). The [iSOSIA](#)
1456 version [spm-3.3.3r](#) glacier model is available from Zenodo (Rowan and Pedersen, 2024).

Deleted: is available on GitHub
(<https://github.com/cryotools/cosipy>).

Deleted: of the

Deleted: used in this study

1457 **Data availability**
1458 Daily data from the Coordinated Regional Downscaling Experiment (CORDEX) South Asia domain
1459 were downloaded from the Indian Institute of Tropical Meteorology website
1460 (http://cccr.tropmet.res.in/home/cordexsa_about.jsp) for the grid box nearest to Khumbu Glacier
1461 (27.9065°N, 86.4353°E). Incoming shortwave and longwave radiation components were downloaded
1462 from the ESGF portal (<https://esgf-ui.ceda.ac.uk/cog/projects/cordex-ceda/>). 14 years of meteorological
1463 observations were derived from the two Pyramid AWS at 5,050 m a.s.l. and at 5,035 m a.s.l. (SHARE
1464 network Ev-K2-CNR; <https://www.evk2cnr.org>) and the West Changri Nup glacier AWS at 5,363 m
1465 a.s.l. (GlacioClim; <https://glacioclim.osug.fr/>).

Formatted: Font colour: Auto

Formatted: Font colour: Auto

Formatted: Font colour: Auto

1466 **Author contributions**
1467 Conceptualisation: DJQ, ANR, AVR
1468 Data curation: ASD, ANR, AVR
1469 Formal analysis: ASD, ANR, AVR
1470 Funding acquisition: DJQ, ANR, AVR
1471 Investigation: ASD
1472 Methodology: ASD, ANR, AVR, VKP
1473 Project administration: DJQ, ANR
1474 Resources: DJQ, ANR
1475 Software: AVR, VKP
1476 Supervision: DJQ, ANR, AVR
1477 Validation: ASD, AVR
1478 Visualisation: ASD, AVR
1479 Writing – original draft preparation: ASD, AVR, DJQ, ANR, VKP
1480 Writing – review and editing: ASD, AVR, DJQ, ANR, VKP

1481 **Competing interests**
1482 The authors declare that they have no conflict of interest.

1483 **Acknowledgements**
1484 Tobias Sauter and Anselm Arndt are thanked for support in using COSIPY. We thank Patrick Wagnon
1485 for sharing the Pyramid and Changri Nup Glacier automatic weather station data. We thank David
1486 Rounce for sharing global glacier model results for Khumbu Glacier from Rounce et al. (2023). Some
1487 of the simulations presented were performed on resources provided by Sigma2, the National
1488 Infrastructure for High-Performance Computing and Data Storage in Norway.

1489 **Financial support**
1490 ASD was supported by the Priestley International Centre for Climate at the University of Leeds, and a
1491 University of Leeds Anniversary Research Scholarship. AVR was supported by a Royal Society
1492 Dorothy Hodgkin Research Fellowship (DHF\R1\201113).

1493 **References**
1494 Altena, B. and Kääh, A.: Ensemble matching of repeat satellite images applied to measure fast-changing
1495 ice flow, verified with mountain climber trajectories on Khumbu icefall, Mount Everest, J.
1496 Glaciol., 66, 905–915, <https://doi.org/10.1017/jog.2020.66>, 2020.
1497 [Arndt, A., Sauter, T., Saß, B. \(2020\). cryotools/cosipy: COSIPY v1.3 – An open-source coupled
1498 snowpack and ice surface energy and mass balance model \(v1.3\). Zenodo.
1499 <https://doi.org/10.5281/zenodo.3902191>](#)

- 1511 Anderson, L. S. and Anderson, R. S.: Modeling debris-covered glaciers: response to steady debris
1512 deposition, *The Cryosphere*, 10, 1105–1124, <https://doi.org/10.5194/tc-10-1105-2016>, 2016.
- 1513 Bartlett, O. T., Ng, F. S. L., and Rowan, A. V.: Morphology and evolution of supraglacial hummocks on
1514 debris-covered Himalayan glaciers, *Earth Surf. Process. Landforms*, 46, 525–539,
1515 <https://doi.org/10.1002/esp.5043>, 2021.
- 1516 Benn, D. I. and Lehmkuhl, F.: Mass balance and equilibrium-line altitudes of glaciers in high-mountain
1517 environments, *Quaternary International*, 65–66, 15–29, [https://doi.org/10.1016/S1040-6182\(99\)00034-8](https://doi.org/10.1016/S1040-6182(99)00034-8), 2000.
- 1519 Benn, D. I. and Owen, L. A.: The role of the Indian summer monsoon and the mid-latitude westerlies
1520 in Himalayan glaciation: review and speculative discussion, *Journal of the Geological Society*,
1521 155, 353–363, <https://doi.org/10.1144/gsjgs.155.2.0353>, 1998. ▲
- 1522 [H. Biemans, L.H. Speelman, F. Ludwig, E.J. Moors, A.J. Wiltshire, P. Kumar, D. Gerten, P. Kabat](#)
1523 [\(2013\) Future water resources for food production in five South Asian river basins and potential](#)
1524 [for adaptation—A modeling study, *Science of The Total Environment*,](#)
1525 <https://doi.org/10.1016/j.scitotenv.2013.05.092>.
- 1526 Bonekamp, P. N. J., Wanders, N., Wiel, K., Lutz, A. F., and Immerzeel, W. W.: Using large ensemble
1527 modelling to derive future changes in mountain specific climate indicators in a 2 and 3°C warmer
1528 world in High Mountain Asia, *Int J Climatol*, 41, <https://doi.org/10.1002/joc.6742>, 2021.
- 1529 Bookhagen, B. and Burbank, D. W.: Topography, relief, and TRMM-derived rainfall variations along
1530 the Himalaya, *Geophys. Res. Lett.*, 33, L08405, <https://doi.org/10.1029/2006GL026037>, 2006. ▲
- 1531 [Brock, B.W., Willis, I.C. and Sharp, M.J., 2006. Measurement and parameterization of aerodynamic](#)
1532 [roughness length variations at Haut Glacier d’Arolla, Switzerland. *Journal of Glaciology*,](#)
1533 [52\(177\), pp.281-297. https://doi.org/10.3189/172756506781828746](#)
- 1534 Brun, F., King, O., Réveillet, M., Amory, C., Planchet, A., Berthier, E., Dehecq, A., Bolch, T., Fourteau,
1535 K., Brondeux, J., Dumont, M., Mayer, C., Leins, S., Hugonnet, R., and Wagnon, P.: Everest South
1536 Col Glacier did not thin during the period 1984–2017, *The Cryosphere*, 17, 3251–3268,
1537 <https://doi.org/10.5194/tc-17-3251-2023>, 2023.
- 1538 Collins, M., Knutti, R., and Arblaster, J.: Long-term Climate Change: Projections, Commitments and
1539 Irreversibility. In: *Climate Change 2013: The Physical Science Basis. Contribution of Working*
1540 *Group I to the Fifth Assessment Report of the Intergovernmental Panel on Climate Change*
1541 [Stocker, T.F., D. Qin, G.-K. Plattner, M. Tignor, S.K. Allen, J. Boschung, A. Nauels, Y. Xia, V.
1542 Bex and P.M. Midgley (eds.)]. Cambridge University Press, Cambridge, United Kingdom and
1543 New York, NY, USA., 1–108., 2013.
- 1544 Compagno, L., Huss, M., Miles, E. S., McCarthy, M. J., Zekollari, H., Dehecq, A., Pellicciotti, F., and
1545 Farinotti, D.: Modelling supraglacial debris-cover evolution from the single-glacier to the
1546 regional scale: an application to High Mountain Asia, *The Cryosphere*, 16, 1697–1718,
1547 <https://doi.org/10.5194/tc-16-1697-2022>, 2022. ▲
- 1548 [Cuffey, K.M. and Paterson, W.S.B., 2010. *The physics of glaciers*. Academic Press.](#)
- 1549 Dehecq, A., Gourmelen, N., Gardner, A. S., Brun, F., Goldberg, D., Nienow, P. W., Berthier, E., Vincent,
1550 C., Wagnon, P., and Trouvé, E.: Twenty-first century glacier slowdown driven by mass loss in
1551 High Mountain Asia, *Nature Geosci*, 12, 22–27, <https://doi.org/10.1038/s41561-018-0271-9>,
1552 2019.
- 1553 Egholm, D. L., Knudsen, M. F., Clark, C. D., and Lesemann, J. E.: Modeling the flow of glaciers in
1554 steep terrains: The integrated second-order shallow ice approximation (iSOSIA), *J. Geophys.*
1555 *Res.*, 116, <https://doi.org/10.1029/2010JF001900>, 2011.
- 1556 Farinotti, D., Huss, M., Fürst, J. J., Landmann, J., Machguth, H., Maussion, F., and Pandit, A.: A
1557 consensus estimate for the ice thickness distribution of all glaciers on Earth, *Nat. Geosci.*, 12,
1558 168–173, <https://doi.org/10.1038/s41561-019-0300-3>, 2019.
- 1559 Farr, T. G., Rosen, P. A., Caro, E., Crippen, R., Duren, R., Hensley, S., Kobrick, M., Paller, M.,
1560 Rodriguez, E., Roth, L., Seal, D., Shaffer, S., Shimada, J., Umland, J., Werner, M., Oskin, M.,
1561 Burbank, D., and Alsdorf, D.: The Shuttle Radar Topography Mission, *Reviews of Geophysics*,
1562 45, 2005RG000183, <https://doi.org/10.1029/2005RG000183>, 2007.
- 1563 Ferguson, J. and Vieli, A.: Modelling steady states and the transient response of debris-covered glaciers,
1564 [Cryosphere](#), <https://doi.org/10.5194/tc-2020-228>, 2020.

Formatted: Font: +Body (Calibri), 12 pt

Formatted: Font: +Body (Calibri), 12 pt

Formatted: Font: +Body (Calibri), 12 pt

Deleted: coveredglaciers

1566 Förster, K., Hanzer, F., Winter, B., Marke, T., and Strasser, U.: An open-source MEteoroLOGical
1567 observation time series DISaggregation Tool (MELODIST v0.1.1), *Geosci. Model Dev.*, 9, 2315–
1568 2333, <https://doi.org/10.5194/gmd-9-2315-2016>, 2016.

1569 Gades, A., Conway, H., Nereson, N., Naito, N., and Kadota, T.: Radio echo-sounding through
1570 supraglacial debris on Lirung and Khumbu Glaciers, Nepal Himalayas, *Debris-Covered Glaciers*
1571 (Proceedings of a workshop held at Seattle, Washington, USA, September 2000). IAHS, 264, 13–
1572 22, 2000.

1573 Gao, Y., Chen, F., Lettenmaier, D. P., Xu, J., Xiao, L., and Li, X.: Does elevation-dependent warming
1574 hold true above 5000 m elevation? Lessons from the Tibetan Plateau, *npj Clim Atmos Sci*, 1, 19,
1575 <https://doi.org/10.1038/s41612-018-0030-z>, 2018.

1576 Gromke, C., Manes, C., Walter, B., Lehning, M. and Guala, M., 2011. Aerodynamic roughness length
1577 of fresh snow. *Boundary-Layer Meteorology*, 141, pp.21-34. [https://doi.org/10.1007/s10546-
1578 011-9623-3](https://doi.org/10.1007/s10546-011-9623-3)

1579 Guo, S., Chen, R., Liu, G., Han, C., Song, Y., Liu, J., Yang, Y., Liu, Z., Wang, X., Liu, X. and Wang, L.,
1580 2018. Simple parameterization of aerodynamic roughness lengths and the turbulent heat fluxes
1581 at the top of midlatitude August-One Glacier, Qilian Mountains, China. *Journal of Geophysical
1582 Research: Atmospheres*, 123(21), pp.12-066. <https://doi.org/10.1029/2018JD028875>

1583 Herreid, S. and Pellicciotti, F.: The state of rock debris covering Earth's glaciers, *Nat. Geosci.*, 13, 621–
1584 627, <https://doi.org/10.1038/s41561-020-0615-0>, 2020.

1585 Hornsey, J., Rowan, A. V., Kirkbride, M. P., Livingstone, S. J., Fabel, D., Rodes, A., Quincey, D. J.,
1586 Hubbard, B., and Jomelli, V.: Be-10 Dating of Ice-Marginal Moraines in the Khumbu Valley,
1587 Nepal, Central Himalaya, Reveals the Response of Monsoon-Influenced Glaciers to Holocene
1588 Climate Change, *JGR Earth Surface*, 127, <https://doi.org/10.1029/2022JF006645>, 2022.

1589 Huintjes, E., Neckel, N., Hochschild, V., and Schneider, C.: Surface energy and mass balance at
1590 Purogangri ice cap, central Tibetan Plateau, 2001–2011, *J. Glaciol.*, 61, 1048–1060,
1591 <https://doi.org/10.3189/2015JoG15J056>, 2015.

1592 Immerzeel, W. W., van Beek, L. P. H., Konz, M., Shrestha, A. B., and Bierkens, M. F. P.: Hydrological
1593 response to climate change in a glacierized catchment in the Himalayas, *Climatic Change*, 110,
1594 721–736, <https://doi.org/10.1007/s10584-011-0143-4>, 2012.

1595 Irvine-Fynn, T.D., Sanz-Ablanedo, E., Rutter, N., Smith, M.W. and Chandler, J.H., 2014. Measuring
1596 glacier surface roughness using plot-scale, close-range digital photogrammetry. *Journal of
1597 Glaciology*, 60(223), pp.957-969. doi:10.3189/2014JoG14J032

1598 Jouvet, G., Huss, M., Funk, M., and Blatter, H.: Modelling the retreat of Grosse Aletschgletscher,
1599 Switzerland, in a changing climate, *J. Glaciol.*, 57, 1033–1045,
1600 <https://doi.org/10.3189/002214311798843359>, 2011.

1601 Kaini, S., Nepal, S., Pradhananga, S., Gardner, T. and Sharma, A. K. (2019) Representative general
1602 circulation models selection and downscaling of climate data for the transboundary Koshi river
1603 basin in China and Nepal. *International Journal of Climatology*, 40(9): 4131-4149. doi:
1604 10.1002/joc.6447.

1605 Katzenberger, A., Schewe, J., Pongratz, J., and Levermann, A.: Robust increase of Indian monsoon
1606 rainfall and its variability under future warming in CMIP6 models, *Earth Syst. Dynam.*, 12, 367–
1607 386, <https://doi.org/10.5194/esd-12-367-2021>, 2021.

1608 Khadka, A., Matthews, T., Perry, L. B., Koch, I., Wagnon, P., Shrestha, D., Sherpa, T. C., Aryal, D., Tait,
1609 A., Sherpa, T. G., Tuladhar, S., Baidya, S. K., Elvin, S., Elmore, A. C., Gajurel, A., and Mayewski,
1610 P. A.: Weather On MOUNT EVEREST During The 2019 Summer MONSOON, *Weather*, 76, 205–
1611 207, <https://doi.org/10.1002/wea.3931>, 2021.

1612 King, O., Bhattacharya, A., Ghuffar, S., Tait, A., Guilford, S., Elmore, A. C., and Bolch, T.: Six Decades
1613 of Glacier Mass Changes around Mt. Everest Are Revealed by Historical and Contemporary
1614 Images, *One Earth*, 3, 608–620, <https://doi.org/10.1016/j.oneear.2020.10.019>, 2020.

1615 Knap, W.H. and Oerlemans, J., 1996. The surface albedo of the Greenland ice sheet: satellite-derived
1616 and in situ measurements in the Sondre Strømfjord area during the 1991 melt season. *Journal of
1617 Glaciology*, 42(141), pp.364-374. doi:10.3189/S0022143000004214

Formatted: Font: +Body (Calibri), 12 pt

Formatted: Font: +Body (Calibri), 12 pt

Deleted: on

Deleted: during the

Deleted: summer MONSOON

- 1622 Kraaijenbrink, P. D. A., Bierkens, M. F. P., Lutz, A. F., and Immerzeel, W. W.: Impact of a global
1623 temperature rise of 1.5 degrees Celsius on Asia's glaciers, *Nature*, 549, 257–260,
1624 <https://doi.org/10.1038/nature23878>, 2017.
- 1625 [Lafon, T., Dadson, S., Buys, G. and Prudhomme, C., 2013. Bias correction of daily precipitation
1626 simulated by a regional climate model: a comparison of methods. *International journal of
1627 climatology*, 33\(6\), pp.1367-1381.](#)
- 1628 [Luo, M., Liu, T., Meng, F., Duan, Y., Frankl, A., Bao, A. and De Maeyer, P. 2018. Comparing bias
1629 correction methods used in downscaling precipitation and temperature from regional climate
1630 models: A case study from the Kaidu River basin in western China. *Water*, 10\(8\), pp. 1046.
1631 <https://doi.org/10.3390/w10081046>](#)
- 1632 [Lutz, A.F., Immerzeel, W.W., Kraaijenbrink, P.D., Shrestha, A.B. and Bierkens, M.F., 2016. Climate
1633 change impacts on the upper Indus hydrology: sources, shifts and extremes. *PLoS one*, 11\(11\),
1634 p.e0165630.](#)
- 1635 Marzeion, B., Hock, R., Anderson, B., Bliss, A., Champollion, N., Fujita, K., Huss, M., Immerzeel, W.
1636 W., Kraaijenbrink, P., Malles, J., Maussion, F., Radić, V., Rounce, D. R., Sakai, A., Shannon, S.,
1637 Van De Wal, R., and Zekollari, H.: Partitioning the Uncertainty of Ensemble Projections of
1638 Global Glacier Mass Change, *Earth's Future*, 8, e2019EF001470,
1639 <https://doi.org/10.1029/2019EF001470>, 2020.
- 1640 [Maraun, D., 2016. Bias correcting climate change simulations-a critical review. *Current Climate
1641 Change Reports*, 2\(4\), pp.211-220.](#)
- 1642 Matthews, T., Perry, L. B., Koch, I., Aryal, D., Khadka, A., Shrestha, D., Abernathy, K., Elmore, A. C.,
1643 Seimon, A., Tait, A., Elvin, S., Tuladhar, S., Baidya, S. K., Potocki, M., Birkel, S. D., Kang, S.,
1644 Sherpa, T. C., Gajurel, A., and Mayewski, P. A.: Going to Extremes: Installing the World's
1645 Highest Weather Stations on Mount Everest, *Bulletin of the American Meteorological Society*,
1646 101, E1870–E1890, <https://doi.org/10.1175/BAMS-D-19-0198.1>, 2020.
- 1647 Maurer, J. M., Schaefer, J. M., Rupper, S., and Corley, A.: Acceleration of ice loss across the Himalayas
1648 over the past 40 years, *Sci. Adv.*, 5, eaav7266, <https://doi.org/10.1126/sciadv.aav7266>, 2019.
- 1649 Miles, E. S., Willis, I., Buri, P., Steiner, J. F., Arnold, N. S., and Pellicciotti, F.: Surface Pond Energy
1650 Absorption Across Four Himalayan Glaciers Accounts for 1/8 of Total Catchment Ice Loss,
1651 *Geophys. Res. Lett.*, 45, <https://doi.org/10.1029/2018GL079678>, 2018a.
- 1652 Miles, K. E., Hubbard, B., Quincey, D. J., Miles, E. S., Sherpa, T. C., Rowan, A. V., and Doyle, S. H.:
1653 Polythermal structure of a Himalayan debris-covered glacier revealed by borehole thermometry,
1654 *Sci Rep*, 8, 16825, <https://doi.org/10.1038/s41598-018-34327-5>, 2018b.
- 1655 Miles, K. E., Hubbard, B., Miles, E. S., Quincey, D. J., Rowan, A. V., Kirkbride, B., and Hornsey, J.:
1656 Continuous borehole optical televiewing reveals variable englacial debris concentrations at
1657 Khumbu Glacier, Nepal, *Commun Earth Environ*, 2, 12, <https://doi.org/10.1038/s43247-020-00070-x>, 2021.
- 1658 Mölg, T., Maussion, F., [Yang, W. and Scherer, D., 2012. The footprint of Asian monsoon dynamics in
1659 the mass and energy balance of a Tibetan glacier. *The Cryosphere*, 6\(6\), pp.1445-1461.
1660 <https://doi.org/10.5194/tc-6-1445-2012>](#)
- 1661 Mölg, T., Maussion, F., and Scherer, D.: Mid-latitude westerlies as a driver of glacier variability in
1662 monsoonal High Asia, *Nature Clim Change*, 4, 68–73, <https://doi.org/10.1038/nclimate2055>,
1663 2014.
- 1664 Mott, R., Stiperski, I., and Nicholson, L.: Spatio-temporal flow variations driving heat exchange
1665 processes at a mountain glacier, *The Cryosphere*, 14, 4699–4718, <https://doi.org/10.5194/tc-14-4699-2020>, 2020.
- 1666 Nakawo, M.: Processes Which Distribute Supraglacial Debris On The Khumbu Glacier, Nepal
1667 Himalaya, *Annals of Glaciology*, 8, 1986.
- 1668 Nicholson, L., Wirbel, A., Mayer, C., and Lambrecht, A.: The Challenge of Non-Stationary Feedbacks
1669 in Modeling the Response of Debris-Covered Glaciers to Climate Forcing, *Front. Earth Sci.*, 9,
1670 662695, <https://doi.org/10.3389/feart.2021.662695>, 2021.
- 1671 [Oerlemans, J., 2001. *Glaciers and climate change*. CRC Press.](#)
- 1672 Owen, L. A., Robinson, R., Benn, D. I., Finkel, R. C., Davis, N. K., Yi, C., Putkonen, J., Li, D., and
1673 Murray, A. S.: Quaternary glaciation of Mount Everest, *Quaternary Science Reviews*, 28, 1412–
1674 1433, <https://doi.org/10.1016/j.quascirev.2009.02.010>, 2009.

Formatted: Font: +Body (Calibri), 12 pt

Formatted: Font: +Body (Calibri), 12 pt

1677 Pedersen, J. S. T., Van Vuuren, D. P., Aparicio, B. A., Swart, R., Gupta, J., and Santos, F. D.: Variability
1678 in historical emissions trends suggests a need for a wide range of global scenarios and regional
1679 analyses, *Commun Earth Environ*, 1, 41, <https://doi.org/10.1038/s43247-020-00045-y>, 2020.

1680 Pellicciotti, F., Stephan, C., Miles, E., Herreid, S., Immerzeel, W. W., and Bolch, T.: Mass-balance
1681 changes of the debris-covered glaciers in the Langtang Himal, Nepal, from 1974 to 1999, *J.*
1682 *Glaciol.*, 61, 373–386, <https://doi.org/10.3189/2015JoG13J237>, 2015.

1683 Pepin, N. C., Arnone, E., Gobiet, A., Haslinger, K., Kotlarski, S., Notarnicola, C., Palazzi, E., Seibert,
1684 P., Serafin, S., Schöner, W., Terzago, S., Thornton, J. M., Vuille, M., and Adler, C.: Climate
1685 Changes and Their Elevational Patterns in the Mountains of the World, *Reviews of Geophysics*,
1686 60, <https://doi.org/10.1029/2020RG000730>, 2022.

1687 Piani, C., Weedon, G.P., Best, M., Gomes, S.M., Viterbo, P., Hagemann, S. and Haerter, J.O., 2010.
1688 Statistical bias correction of global simulated daily precipitation and temperature for the
1689 application of hydrological models. *Journal of hydrology*, 395(3-4), pp.199-215.
1690 <https://doi.org/10.1016/j.jhydrol.2010.10.024>

1691 Pierce, D. W., Barnett, T. P., Santer, B. D., and Gleckler, P. J.: Selecting global climate models for
1692 regional climate change studies, *Proc. Natl. Acad. Sci. U.S.A.*, 106, 8441–8446,
1693 <https://doi.org/10.1073/pnas.0900094106>, 2009.

1694 Potocki, M., Mayewski, P. A., Matthews, T., Perry, L. B., Schwikowski, M., Tait, A. M., Korotkikh, E.,
1695 Clifford, H., Kang, S., Sherpa, T. C., Singh, P. K., Koch, I., and Birkel, S.: Mt. Everest’s highest
1696 glacier is a sentinel for accelerating ice loss, *npj Clim Atmos Sci*, 5, 7,
1697 <https://doi.org/10.1038/s41612-022-00230-0>, 2022.

1698 Pritchard, H. D.: Asia’s shrinking glaciers protect large populations from drought stress, *Nature*, 569,
1699 649–654, <https://doi.org/10.1038/s41586-019-1240-1>, 2019.

1700 Quincey, D. J., Luckman, A., and Benn, D.: Quantification of Everest region glacier velocities between
1701 1992 and 2002, using satellite radar interferometry and feature tracking, *J. Glaciol.*, 55, 596–606,
1702 <https://doi.org/10.3189/002214309789470987>, 2009.

1703 Ragettli, S., Immerzeel, W. W., and Pellicciotti, F.: Contrasting climate change impact on river flows
1704 from high-altitude catchments in the Himalayan and Andes Mountains, *Proc Natl Acad Sci USA*,
1705 113, 9222–9227, <https://doi.org/10.1073/pnas.1606526113>, 2016.

1706 RGI 7.0 Consortium: A Dataset of Global Glacier Outlines, Version 7.0. Boulder, Colorado USA.
1707 NSIDC: National Snow and Ice Data Center, <https://doi.org/10.5067/f6jmovy5navz>, 2023.

1708 Reiter, P., Gutjahr, O., Schefczyk, L., Heinemann, G. and Casper, M., 2018. Does applying quantile
1709 mapping to subsamples improve the bias correction of daily precipitation?. *International Journal*
1710 *of Climatology*, 38(4), pp.1623-1633.

1711 Roering, J. J., Kirchner, J. W., and Dietrich, W. E.: Evidence for nonlinear, diffusive sediment transport
1712 on hillslopes and implications for landscape morphology, *Water Resources Research*, 35, 853–
1713 870, <https://doi.org/10.1029/1998WR900090>, 1999.

1714 Rounce, D. R., Hock, R., Maussion, F., Hugonnet, R., Kochtitzky, W., Huss, M., Berthier, E.,
1715 Brinkerhoff, D., Compagno, L., Copland, L., Farinotti, D., Menounos, B., and McNabb, R. W.:
1716 Global glacier change in the 21st century: Every increase in temperature matters, *Science*, 379,
1717 78–83, <https://doi.org/10.1126/science.abo1324>, 2023.

1718 Rowan, A. V.: The ‘Little Ice Age’ in the Himalaya: A review of glacier advance driven by Northern
1719 Hemisphere temperature change, *The Holocene*, 27, 292–308,
1720 <https://doi.org/10.1177/0959683616658530>, 2017.

1721 Rowan, A. V., Egholm, D. L., Quincey, D. J., and Glasser, N. F.: Modelling the feedbacks between mass
1722 balance, ice flow and debris transport to predict the response to climate change of debris-covered
1723 glaciers in the Himalaya, *Earth and Planetary Science Letters*, 430, 427–438,
1724 <https://doi.org/10.1016/j.epsl.2015.09.004>, 2015.

1725 Rowan, A. V., Egholm, D. L., Quincey, D. J., Hubbard, B., King, O., Miles, E. S., Miles, K. E., and
1726 Hornsey, J.: The Role of Differential Ablation and Dynamic Detachment in Driving Accelerating
1727 Mass Loss From a Debris-Covered Himalayan Glacier, *J. Geophys. Res. Earth Surf.*, 126,
1728 <https://doi.org/10.1029/2020JF005761>, 2021.

1729 Rowan, A., & Pedersen, V. K. (2024). *annvrowan/isosia: iSOSIA version used in Schlich-Davies et al.*
1730 *(spm-3.3.3r)*. Zenodo. <https://doi.org/10.5281/zenodo.12666864>

Formatted: Font: +Body (Calibri), 12 pt

Formatted: Font: +Body (Calibri), 12 pt

Formatted: Font: +Body (Calibri), 12 pt

1731 Salerno, F., Guyennon, N., Yang, K., Shaw, T. E., Lin, C., Colombo, N., Romano, E., Gruber, S., Bolch,
1732 T., Alessandri, A., Cristofanelli, P., Putero, D., Diolaiuti, G., Tartari, G., Verza, G., Thakuri, S.,
1733 Balsamo, G., Miles, E. S., and Pellicciotti, F.: Local cooling and drying induced by Himalayan
1734 glaciers under global warming, *Nat. Geosci.*, 16, 1120–1127, [https://doi.org/10.1038/s41561-](https://doi.org/10.1038/s41561-023-01331-y)
1735 023-01331-y, 2023.

1736 Sanjay, J., Krishnan, R., Shrestha, A. B., Rajbhandari, R., and Ren, G.-Y.: Downscaled climate change
1737 projections for the Hindu Kush Himalayan region using CORDEX South Asia regional climate
1738 models, *Advances in Climate Change Research*, 8, 185–198,
1739 <https://doi.org/10.1016/j.accre.2017.08.003>, 2017.

1740 Sauter, T., Arndt, A., and Schneider, C.: COSIPY v1.3 – an open-source coupled snowpack and ice
1741 surface energy and mass balance model, *Geosci. Model Dev.*, 13, 5645–5662,
1742 <https://doi.org/10.5194/gmd-13-5645-2020>, 2020.

1743 Shaw, T. E., Miles, E. S., Chen, D., Jouberton, A., Kneib, M., Fugger, S., Ou, T., Lai, H.-W., Fujita, K.,
1744 Yang, W., Fatichi, S., and Pellicciotti, F.: Multi-decadal monsoon characteristics and glacier
1745 response in High Mountain Asia, *Environ. Res. Lett.*, 17, 104001, [https://doi.org/10.1088/1748-](https://doi.org/10.1088/1748-9326/ac9008)
1746 9326/ac9008, 2022.

1747 Shaw, T. E., Buri, P., McCarthy, M., Miles, E. S., and Pellicciotti, F.: Local Controls on Near-Surface
1748 Glacier Cooling Under Warm Atmospheric Conditions, *JGR Atmospheres*, 129, e2023JD040214,
1749 <https://doi.org/10.1029/2023JD040214>, 2024.

1750 Shea, J. M., Immerzeel, W. W., Wagnon, P., Vincent, C., and Bajracharya, S.: Modelling glacier change
1751 in the Everest region, Nepal Himalaya, *The Cryosphere*, 9, 1105–1128,
1752 <https://doi.org/10.5194/tc-9-1105-2015>, 2015.

1753 [Sherpa, S. F., Wagnon, P., Brun, F., Berthier, E., Vincent, C., Lejeune, Y., et al. \(2017\). Contrasted](#)
1754 [surface mass balances of debris-free glaciers observed between the southern and the inner parts](#)
1755 [of the Everest region \(2007–15\). *Journal of Glaciology*, 63\(240\), 637–651.](#)
1756 <https://doi.org/10.1017/jog.2017.30>

1757 Strickland, R. M., Covington, M. D., Gulley, J. D., Kayastha, R. B., and Blackstock, J. M.: Englacial
1758 Drainage Drives Positive Feedback Depression Growth on the Debris-Covered Ngozumpa
1759 Glacier, Nepal, *Geophysical Research Letters*, 50, e2023GL104389,
1760 <https://doi.org/10.1029/2023GL104389>, 2023.

1761 Vacco, D. A., Alley, R. B., and Pollard, D.: Glacial advance and stagnation caused by rock avalanches,
1762 *Earth and Planetary Science Letters*, 294, 123–130, <https://doi.org/10.1016/j.epsl.2010.03.019>,
1763 2010.

1764 [Wagnon, P., Lafaysse, M., Lejeune, Y., Maisincho, L., Rojas, M. and Chazarin, J.P., 2009.](#)
1765 [Understanding and modeling the physical processes that govern the melting of snow cover in a](#)
1766 [tropical mountain environment in Ecuador. *Journal of Geophysical Research: Atmospheres*,](#)
1767 [114\(D19\).](#)

1768 Watson, C. S., Quincey, D. J., Smith, M. W., Carrivick, J. L., Rowan, A. V., and James, M. R.:
1769 Quantifying ice cliff evolution with multi-temporal point clouds on the debris-covered Khumbu
1770 Glacier, Nepal, *J. Glaciol.*, 63, 823–837, <https://doi.org/10.1017/jog.2017.47>, 2017.

1771 [Weidemann, S.S., Sauter, T., Malz, P., Jaña, R., Arigony-Neto, J., Casassa, G. and Schneider, C. \(2018\).](#)
1772 [Glacier Mass Changes of Lake-Terminating Grey and Tyndall Glaciers at the Southern Patagonia](#)
1773 [Icefield Derived From Geodetic Observations and Energy and Mass Balance Modeling. *Frontiers*](#)
1774 [in Earth Science](#), 6: 81. doi: 10.3389/feart.2018.00081.

1775 Wirbel, A., Jarosch, A. H., and Nicholson, L.: Modelling debris transport within glaciers by advection
1776 in a full-Stokes ice flow model, *The Cryosphere*, 12, 189–204, [https://doi.org/10.5194/tc-12-189-](https://doi.org/10.5194/tc-12-189-2018)
1777 2018, 2018.

1778 Zekollari, H., Huss, M., Farinotti, D., and Lhermitte, S.: Ice-Dynamical Glacier Evolution Modeling—
1779 A Review, *Reviews of Geophysics*, 60, <https://doi.org/10.1029/2021RG000754>, 2022.

Formatted: Font: +Body (Calibri), 12 pt

Formatted: Font: +Body (Calibri), 12 pt

1781

1782
1783
1784
1785
1786
1787
1788
1789
1790

Tables and captions

Table 1. Regional Climate Models (RCMs) chosen for this study and details of the Global Circulation Models (GCMs) from which these are derived. The NOAA RCM that was considered most representative of conditions in the Everest region. The temperature forcings used to project climate change beyond 2100 CE are global values (they are simply included against each of the RCMs for ease comparing with 2100 temperature change) and include no change in precipitation after 2100 CE.

Deleted: Table
Deleted: caption
Formatted: Font: 11 pt
Formatted: Font: 11 pt

CORDEX South Asia regional climate model	Driving CMIP5 global climate model	CMIP5 modelling centre	RCM name in this study	Future precipitation scenario (qualitative)	2100 CE mean temperature change from present day (°C)		2200 CE mean temperature change from 2100 CE (°C)		2300 CE mean temperature change from 2100 CE (°C) /2200CE	
					RCP 4.5	RCP 8.5	RCP 4.5	RCP 8.5	RCP 4.5	RCP 8.5
JTMM-RegCM4	NOAA-GFDL-GFDL-ESM2M	National Oceanic and Atmospheric Administration (NOAA), USA	NOAA	Wet	1.4	3.8	0.5	2.8	0.7 /0.2	4.1 /1.3
JTMM-RegCM4	CCCma-CanESM2	Canadian Centre for Climate Modelling and Analysis (CCCma), Canada	CCCma	Moderate	2.2	4.1	0.5	2.8	0.7	4.1
JTMM-RegCM4	IPSL-CM5A-LR	Institut Pierre-Simon Laplace (IPSL), France	IPSL	Dry	1.6	3.8	0.5	2.8	0.7	4.1

Formatted: Font colour: Auto
Formatted: Font colour: Auto
Formatted: Font colour: Auto
Formatted: Font colour: Auto

1791
1792
1793
1794
1795
1796
1797
1798

Table 2: Model parameters, where α is albedo (of fresh snow, firn and ice), t^* decay time from snow to firn, d^* the constant for the effect of snow depth on albedo, and z_0 surface roughness length. The albedo values are widely used within the literature for clean. z_0 values are less well parameterised with high spatial variability across glacier surfaces. Testing revealed highest sensitivity of mass balance to $\alpha_{freshsnow}$ relative to the other parameters.

Formatted: Font: 11 pt
Formatted: Justified
Formatted: Font: 11 pt
Formatted: Font: 11 pt

Parameter	Value	Unit	Source
$\alpha_{freshsnow}$	0.85	-	Mölg et al. 2012; Wagnon et al., 2009
α_{firn}	0.6	-	Knap and Oerlemans, 1996; Mölg et al. 2012
α_{ice}	0.3	=	Mölg et al. 2012
t^*	20	days	Mölg et al. 2012
d^*	1.0	cm	Mölg et al. 2012
Z_{0snow}	0.24	mm	Gromke et al., 2011
Z_{0firn}	4.0	mm	Brock et al., 2006
Z_{0ice}	1.7	mm	Brock et al., 2006
Z_0 ageing length (linearly from Z_{0snow} to Z_{0firn})	60	days	Mölg et al. 2012

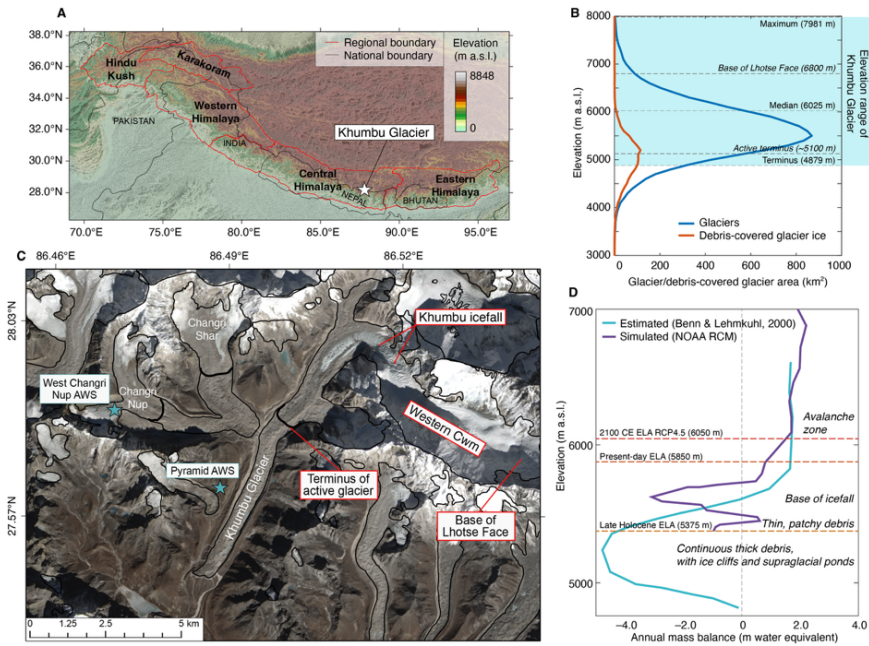
Formatted Table
Moved (insertion) [22]
Formatted Table

1799

1802
1803
1804

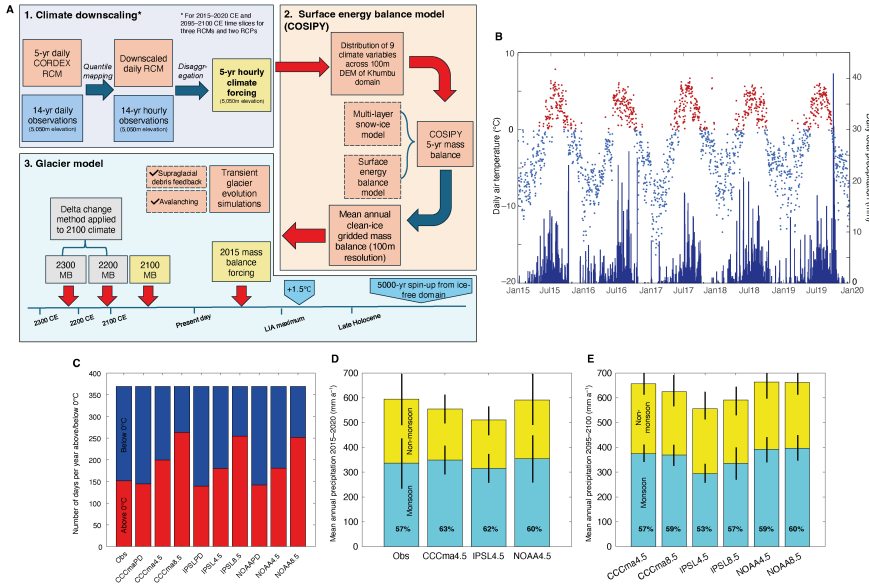
Figures and captions

Formatted: Font: 11 pt



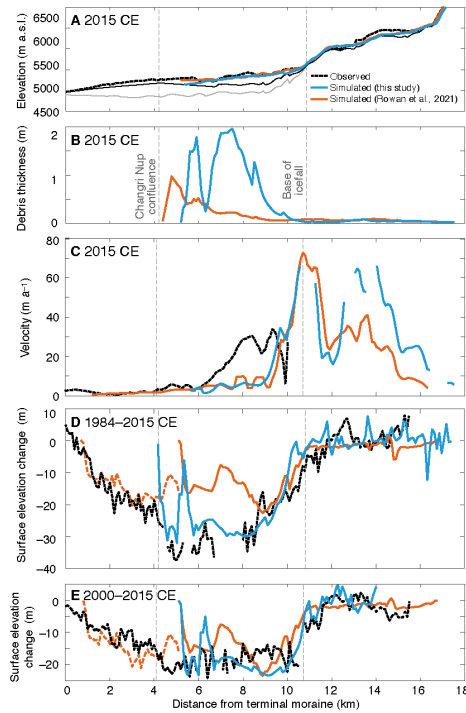
1805
1806
1807
1808
1809
1810
1811
1812
1813
1814
1815
1816
1817
1818
1819
1820
1821

Figure 1: Khumbu Glacier location and context. (a) Location map of High Mountain Asia showing the location of the monsoon-influenced Central and Eastern Himalaya and Khumbu Glacier. (b) hypsometry of glaciers and debris-covered glacier ice in the Central and Eastern Himalaya compared with the elevations of Khumbu Glacier. (c) Satellite image of Khumbu Glacier showing the glacier outline from the RGI database (black line) that is equivalent to the late Holocene (~1 ka) glacier extent identified from ice-marginal moraines, the extent of supraglacial debris, location of the Khumbu Icefall, the extent of active ice flow inferred from observations of glacier velocity, and location of the automatic weather stations used for RCM downscaling (blue stars). (d) Estimated mass balance gradient for debris-covered glaciers in the Everest region (Benn and Lehmkuhl, 2000) compared with the glacier mass balance gradient simulated using the NOAA RCM and showing change in the equilibrium line altitude (ELA) of Khumbu Glacier in the historical and future simulations for the NOAA RCM RCP4.5 experiment.



1822
1823
1824
1825
1826
1827
1828
1829
1830
1831
1832
1833
1834
1835
1836
1837
1838
1839
1840
1841
1842
1843
1844
1845

Figure 2: Glacier model experimental design and evaluation of RCM downscaling. (a) Schematic diagram of the glacier modelling approach showing the methods used for downscaling through quantile mapping and disaggregation of climate data. Note that this process does not apply to the post-2100 CE climate forcings which are subject to delta change. Surface energy balance modelling using COSIPY includes the pre-processing stage of meteorological distribution across the Khumbu domain, which is repeated for each RCM in the 2015–2020 CE climates and for the three RCMs and two RCPs for the 2095–2100 CE climates. The simulated mass balance is then used to force the glacier evolution model. (b) Daily mean temperature and daily total precipitation from the NOAA RCM for the present day (2015–2020 CE) following downscaling using quantile mapping with air temperature categorised into above freezing (red) and below freezing (blue). (c) Proportion of air temperatures above and below freezing for the present day for each RCM and RCP for the downscaled daily data compared with observations. (d) Annual precipitation daily totals for non-monsoon and monsoon with standard deviation between selected years shown by black bars for the downscaled daily data compared with observations. (e) Future (2095–2100 CE) time-slice annual precipitation totals for non-monsoon and monsoon months with standard deviation between selected years shown by black bars. In (d) and (e) the percentage of the total annual precipitation occurring during the monsoon is indicated by the value in bold text. (Obs = meteorological observations from AWS).



1846
1847
1848
1849
1850
1851
1852
1853
1854
1855
1856
1857
1858
1859

Figure 3. Evaluation of present-day simulation showing: (a) mean simulated glacier surface elevation and bed elevation calculated from a 500 m-wide swath profile along the central flowline of the glacier. Subglacial topography including the dynamically detached debris-covered tongue is shown by the solid black line and subglacial topography used in the entire glacier simulations in Rowan et al. (2015) is shown for comparison by the lowermost grey solid line. The estimated present-day ice surface elevation (Farinotti et al., 2019) is shown by the dashed black line. (b) mean simulated debris thickness, (c) simulated and observed velocities from the NASA MEaSUREs ITS LIVE project (Dehecq et al., 2019), and simulated and observed mean surface elevation change between (d) 1984–2015 CE and (e) 2000–2015 CE compared with results from the simulations in this study and those in Rowan et al. (2021) where further information about the model evaluation can be found.

Moved down [23]:
<object><object><object><object>

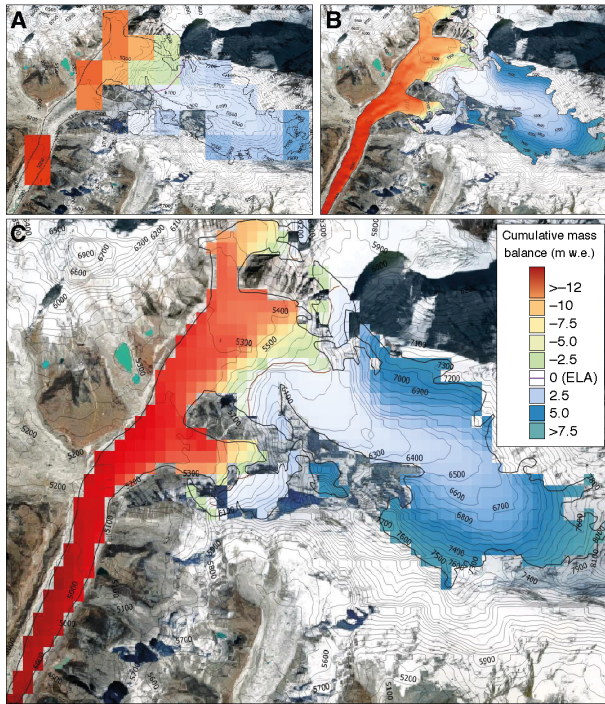
Deleted: Figure 3:

Formatted: Font colour: Auto

Formatted: Font colour: Auto

Formatted: Font: 10 pt, Font colour: Auto, Not Highlight, Ligatures: Standard + Contextual

Formatted: Indent: Left: 0 cm, Space Before: 0 pt, After: 0 pt, Add space between paragraphs of the same style

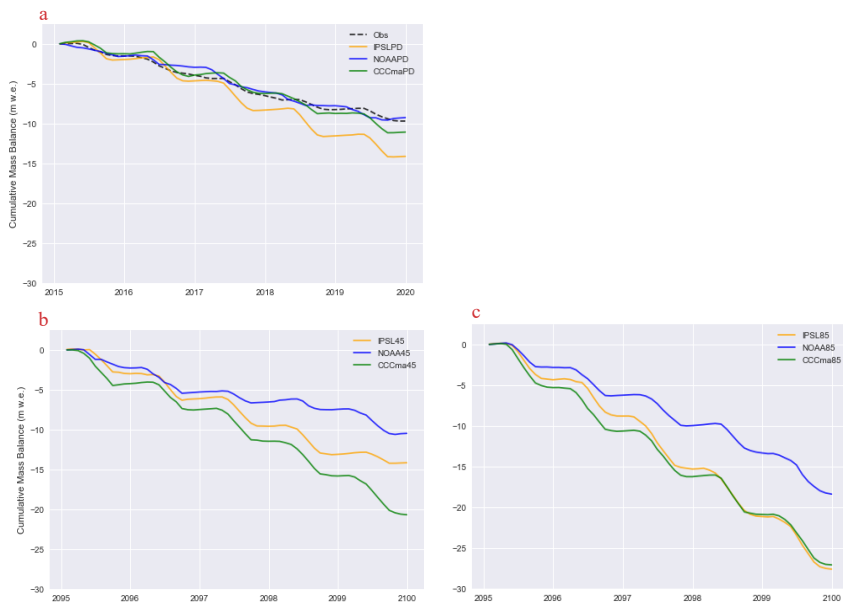


1864
 1865
 1866
 1867
 1868
 1869
 1870

▲
 ▲
 ▲
 ▲
 ▲
 ▲
 ▼

Figure 4. COSIPY reference calculation of present-day mass balance for Khumbu Glacier for the period 2013–2015 CE showing the results from calculations using different grid spacings using (a) a 1-km grid, (b) a 30-m grid, (c) the 200-m grid spacing used throughout the experiments in this study.

- Formatted: Font: 10 pt, Not Bold
- Formatted: Justified
- Formatted: Font: Bold
- Formatted: List Paragraph, Add space between paragraphs of the same style
- Formatted: Font: 11 pt
- Moved (insertion) [23]

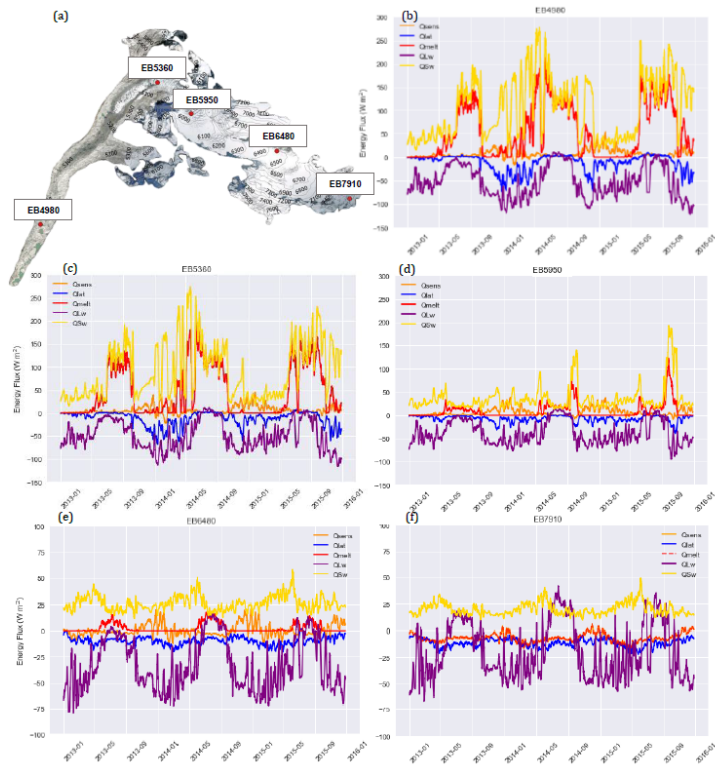


1871
 1872
 1873 **Figure 5.** Spatially averaged cumulative clean-ice mass balance with clear seasonality for (a) the present day
 1874 time-slice including the mass balance forced by the observations used for downscaling, and the end-of-
 1875 century time-slice under (b) RCP4.5 and (c) RCP8.5. The low annual glacier-wide mass balance values
 1876 shown here are the result of the extent of the model domain used to force the glacier model that includes the
 1877 larger catchment beyond the glacier margins and therefore contains a higher proportion of lower elevations
 1878 than those of the glacier itself. However the similar mass balance results for simulations RCM and observations can be clearly seen (a), and the differences between the three RCMs is apparent in
 1879 all time-slices (a-c).
 1880

1881
 1882
 1883
 1884

Formatted: Font: 11 pt

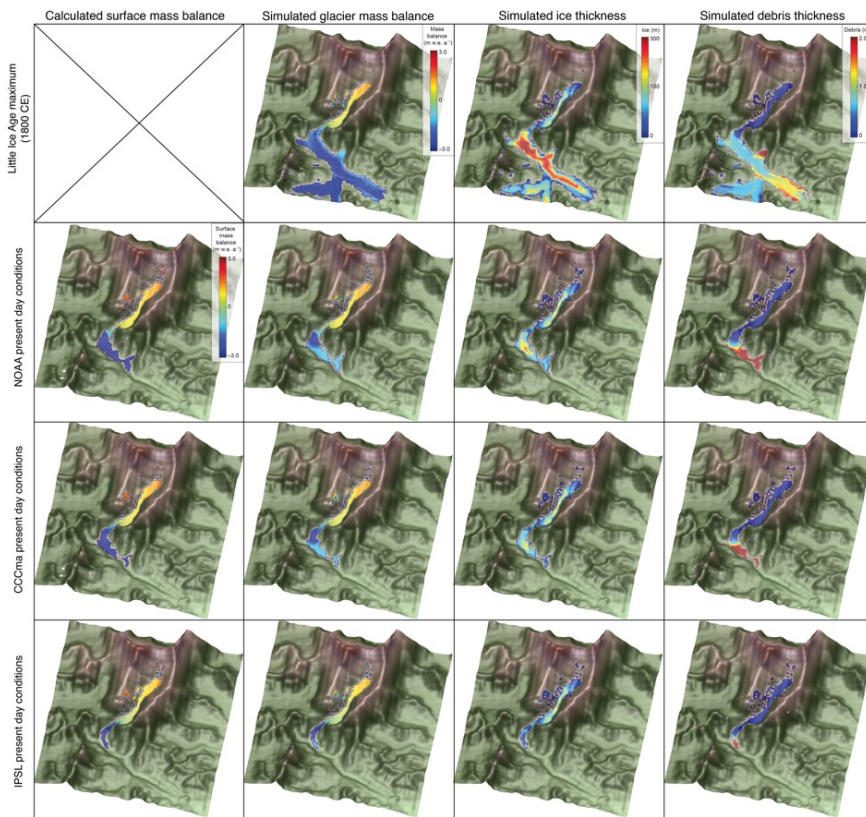
Formatted: Justified



1885
 1886
 1887
 1888
 1889
 1890
 1891
 1892

Figure 6. (a) Locations of energy balance (EB) points used for energy flux and melt components analysis (named after corresponding altitude e.g., EB6480) and (b–f) 5-day average of energy fluxes across study period for each site. Note that scales are different for (e) and (f) compared to (b)–(d) due to the marked difference in absolute values.

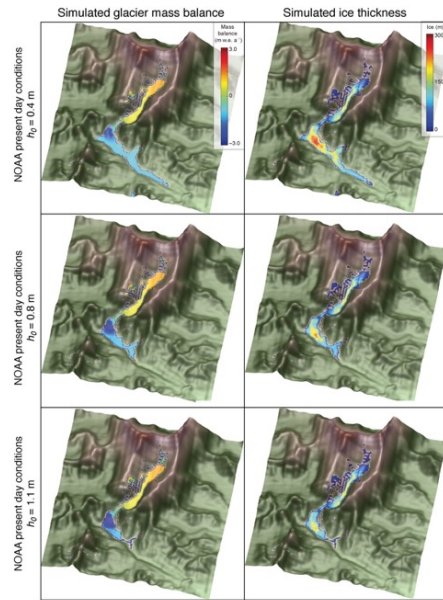
Moved (insertion) [27]



1893
 1894
 1895
 1896
 1897
 1898
 1899
 1900
 1901
 1902
 1903

Figure 7. Glacier model sensitivity to surface energy and mass balance forcing, showing Little Ice Age (~1800 CE) glacier mass balance, ice thickness and debris thickness. Present-day results for surface mass balance calculated using each RCM with COSIPY showing glacier mass balance calculated using the same climate forcing following integration with the glacier model, simulated ice thickness, and simulated debris thickness.

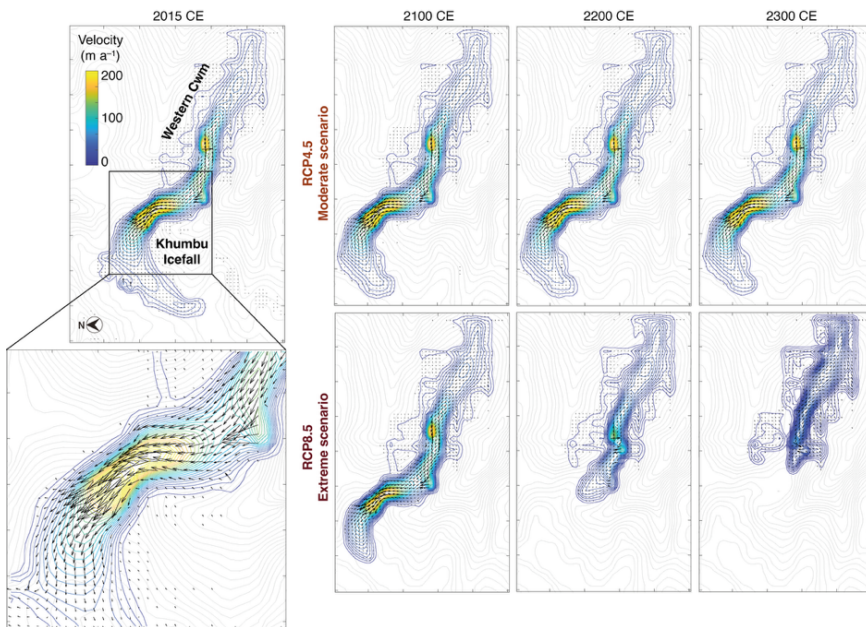
Deleted: 4



1905
 1906
 1907
 1908
 1909
 1910
 1911
 1912
 1913
 1914

Figure 8. Glacier mass balance and ice thickness simulated using the NOAA RCM climate forcing and the resulting simulated ice thickness for h_0 values of 0.4 m, 0.8 m, and 1.1 m where h_0 is a constant in Equation(1) representing the characteristic debris thickness at which the reduction in ablation due to insulation by supraglacial debris is 50% of the value for an equivalent clean-ice surface (Anderson and Anderson, 2016; Rowan et al., 2021).

Deleted: 5



1916
 1917
 1918
 1919
 1920
 1921
 1922
 1923
 1924
 1925
 1926

Figure 9. Simulated ice flow for Khumbu Glacier. Velocity-vector maps showing simulated ice flow magnitude and direction from the present day (2015–2020 CE) until 2300 CE under RCP4.5 and RCP8.5 using the downscaled NOAA climate forcing. Simulated ice flow speed is shown as colour shading with blue contours, and the bed topography is shown by grey contours. The outermost contour in each plot represents the slowest ice flow close to the glacier margins with depth-integrated velocities of 5–10 m a⁻¹. Note that rapid flow across the Western Cwm indicated by one arrow shows the effects of avalanching rather than sustained glacier flow.

Moved (insertion) [28]

Moved (insertion) [29]

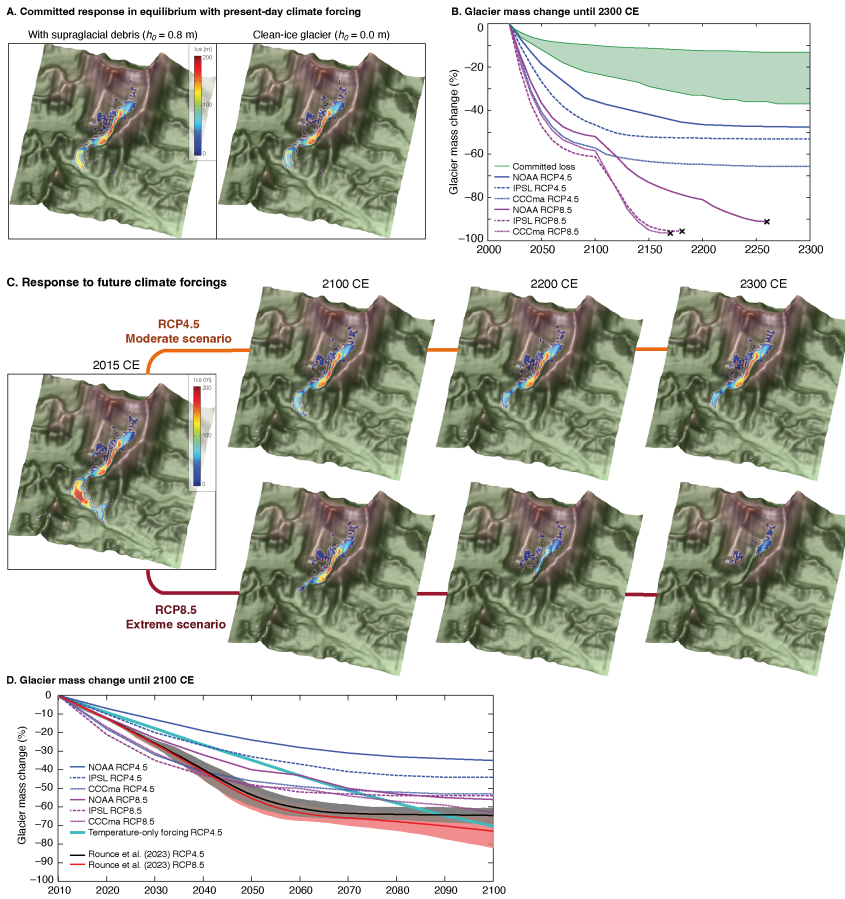


Figure 10. Future glacier volume change projections. (a) Equilibrium ice thickness accounting for the committed response to recent climate change using the downscaled NOAA RCM climate forcing with and without the effect of supraglacial debris on mass balance. (b) Simulated glacier volume change from the present day (2015–2020 CE) until 2300 CE under RCP4.5 and RCP8.5 for the three downscaled RCMs. The black crosses mark when ice flow has declined sufficiently that the glacier is considered almost absent or no longer viable. The green shading shows the range of the committed volume loss due to historical warming. (c) Simulated ice thickness under RCP4.5 and RCP8.5 for 2100 CE, 2200 CE and 2300 CE using the downscaled NOAA RCM climate forcing. (d) Comparison of projected shrinkage of Khumbu Glacier by 2100 CE from this study with those from Rounce et al. (2023) showing results from each of the six experiments in this study with results from RCP4.5 and RCP8.5 from Rounce et al. (2023), the equivalent result for a simulation using a change in MAAT equivalent to the NOAA RCP4.5 forcing where precipitation does not change from the present-day value (cyan line).

Moved up [28]: Simulated ice flow for Khumbu Glacier.

Moved up [29]: Simulated ice flow speed is shown as colour shading with blue contours, and the bed topography is shown by grey contours. The outermost contour in each plot represents the slowest ice flow close to the glacier margins with depth-integrated velocities of 5–10 m a⁻¹. Note that rapid flow across the Western Cwm indicated by one arrow shows the effects of avalanching rather than sustained glacier flow.

Deleted: 6

Deleted: Velocity-vector maps showing simulated ice flow magnitude and direction from the present day (2015–2020 CE) until 2300 CE under RCP4.5 and RCP8.5 using the downscaled NOAA climate forcing and a value for h_0 of 0.8 m where h_0 is a constant in Equation (1) representing the characteristic debris thickness at which the reduction in ... [13]

Deleted: 7

Moved (insertion) [30]

Moved up [30]: (b) Simulated glacier volume change from the present day (2015–2020 CE) until 2300 CE under RCP4.5 and RCP8.5 for the three downscaled RCMs. The black crosses mark when ice flow has declined sufficiently that the glacier is considered almost absent or no longer viable. The green shading shows the range of the committed volume loss

Deleted: sub-debris melt.

Deleted: .

1927
1928
1929
1930
1931
1932
1933
1934
1935
1936
1937
1938
1939
1940
1941
1942
1943
1944

2004
2005
2006
2007
2008
2009
2010
2011
2012
2013
2014
2015
2016
2017
2018
2019
2020
2021
2022
2023
2024
2025
2026
2027
2028
2029

Appendix A: Climate Model Downscaling

This section contains further details on the RCM downscaling, evaluation of the present-day downscaled RCM results using meteorological data, and the distribution of these results across the model domain.

A1. Meteorological data collection and analysis

14 years of meteorological observations were collected from two AWS at the Pyramid Observatory at 5,050 m a.s.l. and 5,035 m a.s.l., and the West Changri Nup Glacier AWS at 5,363 m a.s.l.. Missing data were replaced through interpolation with an alternative AWS from this group. Precipitation was measured at 15-minute intervals using a Geonor T-200BM sensor mounted 1.8 m above the surface. Evaporation from the bucket is supposedly blocked by a layer of oil but some does occur as evidenced by precipitation values below 0 mm. Noise from wind and evaporation were corrected for by compensating any negative change over the 15-minute time step with the neighbouring positive value such that accumulated precipitation was unchanged. Periods with prolonged evaporation were set to zero. Undercatch of snowfall by rainfall gauges was corrected through precipitation phase partitioning using wind speed observations (Wagnon et al., 2009). For interpolation of air temperature, hourly lapse rates were used that averaged $5.54\text{ }^{\circ}\text{C km}^{-1}$ to adjust to the height of the reference point at 5,050 m a.s.l.. Where possible, precipitation data taken from the Pyramid AWS at 5,035 m a.s.l. because this precipitation gauge provides a longer period of continuous observations than the other gauges and avoids errors due to low precipitation amounts measured by tipping bucket gauges, which are known to systematically underestimate snowfall particularly during high winds (Sherpa et al., 2017).

A1. Downscaled climate model results

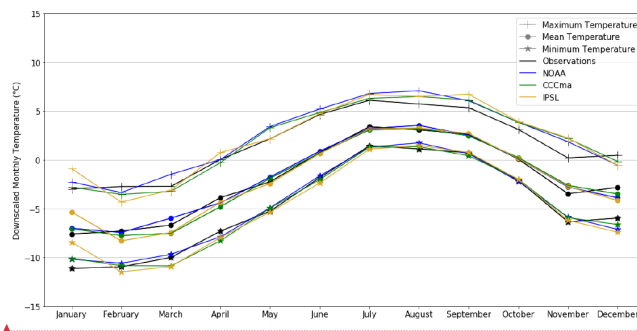


Figure A1: Downscaled monthly mean, maximum, and minimum temperature calculated for the present day time slice.

2030
2031
2032
2033
2034
2035
2036
2037
2038

Moved (insertion) [10]

Moved (insertion) [11]

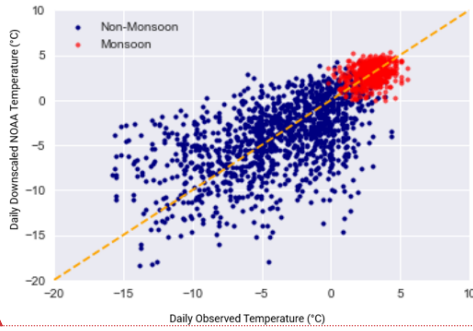
Deleted: 1

Formatted: Font colour: Auto

Formatted: Font colour: Auto

Formatted: Font: 11 pt, Font colour: Auto

Formatted: Font colour: Auto



Formatted: Font colour: Auto

2040
2041
2042
2043
2044
2045
2046
2047
2048

Figure A2: Daily downscaled temperature from the NOAA RCM against observations, split by monsoon/non-monsoon with a 1:1 line to aid analysis of the temperature distributions (dashed orange line).

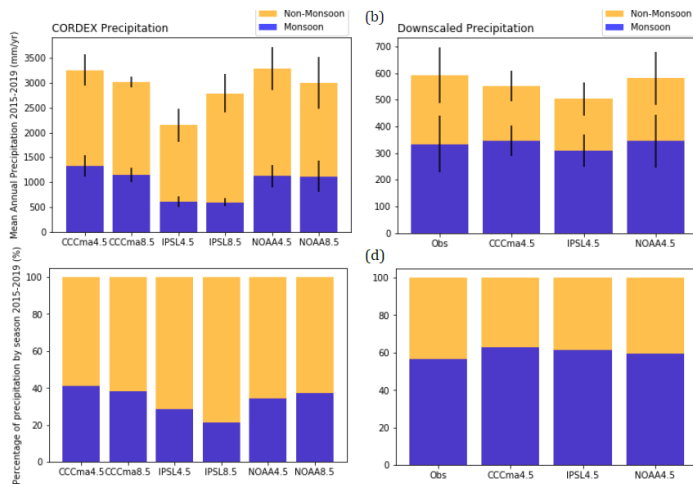
Formatted: Font colour: Auto

Formatted: Justified

Formatted: Font: 11 pt, Font colour: Auto

Formatted: Font colour: Auto

Formatted: Font: 11 pt, Font colour: Auto



2049
2050
2051
2052
2053
2054
2055
2056
2057

Figure A3. Annual precipitation totals for non-monsoon and monsoon months before and after downscaling with standard deviation between selected years shown by black bars (a and b) and as their seasonal percentages (c and d). The annual precipitation matches measurements in the southern Dudh Koshi catchment for the gridbox nearest to Khumbu Glacier is located at 27.9065056°N, 86.4352951°E which is 2,100 m a.s.l..

Deleted: ¶

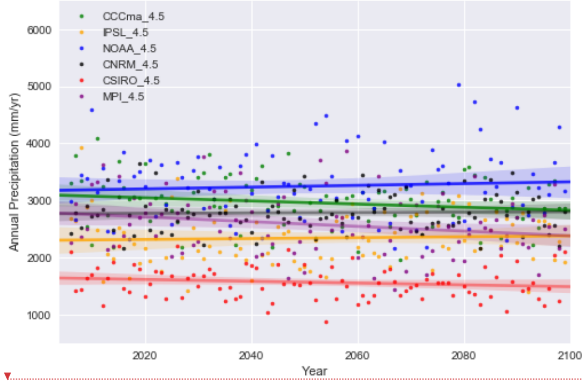
Formatted: Font: 11 pt

A2. Regional Climate Model analysis and selection

Three of the six available CORDEX South Asia RCMs (NOAA, CCCma, IPSL) were selected as discrete scenarios that span the range of possible future precipitation conditions (Table 1); either wet, moderate, or dry climate in 2080–2100 CE (Figure A4). The raw RCMs significantly overestimate annual total precipitation by at least a factor of five for the selected gridpoint which is corrected for by downscaling these results using AWS data.

Deleted: 2

2066



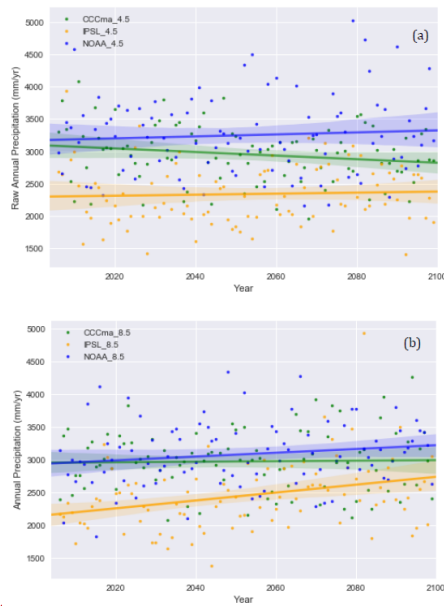
Formatted: Font: 10 pt

Deleted: ¶

2067
2068
2069
2070
2071
2072
2073

Figure A4: Annual precipitation sums (dots) with fitted trend line from the start of the RCP experiments (2006) until the end (2100) for each of the six Indian Institute for Tropical Meteorology CORDEX models for RCP4.5.

Formatted: Font: 11 pt



Formatted: Font colour: Auto

2074
2075
2076
2077
2078
2079
2080
2081

Figure A5: Annual precipitation sums (dots) with fitted trend line from the start of the RCP experiments (2006) until the end (2100) for the three selected of the six CORDEX models for RCP4.5 (a) and 8.5 (b).

Formatted: Font colour: Auto

Formatted: Font: 11 pt

Formatted: Font: 10 pt, Bold

Formatted: Centred, Don't add space between paragraphs of the same style

Formatted: Font colour: Auto

Deleted: 3

2084 **A3. Downscaling parameters and method**
 2085 Though minimum and maximum temperature are not required to force COSIPY, these were downloaded
 2086 and statistically downscaled using QM with normal distribution to aid disaggregation to an hourly time
 2087 step using MELODIST. Quantile mapping for the CORDEX wind speed data was found to be
 2088 ineffective when analysing the time series output against observations, both for the absolute wind speed
 2089 as well as the reduced day-on-day variability seen during the monsoon. Therefore, GARD was used
 2090 instead. This is a simple statistical analogue regression downscaling method appropriate for pointwise
 2091 downscaling.

2092 **Table A1: RCM-derived parameters and the method used for downscaling or bias correction.**

RCM-derived parameters	Downscaling/bias correction method	Parametric distribution model (for QM)	References
Precipitation (kg per m ² per s, converted to mm day ⁻¹)	Quantile mapping (QM)	Gamma	Vrac et al., 2007; Piani et al., 2010
Mean temperature (K) Minimum temperature (K) Maximum temperature (K)	QM	Normal / Gaussian	Li et al., 2010, Gupta et al., 2016; Luo et al., 2018
Incoming shortwave (W m ⁻²) Incoming longwave (W m ⁻²) Relative humidity (%)	QM	Beta	Ruane et al., 2015
Pressure (hPa)	Bias correction	N/A	N/A
Wind speed (m s ⁻¹)	Regression downscaling	N/A	Gutmann et al., 2022

2096 **A4. Meteorological distribution across the model domain**
 2097 Temperature and precipitation were interpolated across the 100-m DEM using a linear relationships:

$$V_{interp} = (V) + (Z_{pixel} - Z_{station}) \cdot LR$$

2103 where V_{interp} is the variable to be interpolated, V is the hourly variable in question (e.g. temperature or
 2104 precipitation), Z_{pixel} is the elevation (m a.s.l.) of the target pixel in the domain, $Z_{station}$ the elevation (m)
 2105 of the station, and LR is the lapse rate for temperature or gradient for precipitation calculated from
 2106 meteorological observations, as described below. Note that the distribution is from a prescribed
 2107 elevation, not from the exact location of the AWS.

2109 The mass balance sensitivity to lapse rate that differed depending on season or time of day were
 2110 examined, showing a lesser impact on glacier-wide mass balance than in other studies due to the large
 2111 elevation range of Khumbu Glacier where a smaller fraction of the glacier relative to total area is located
 2112 along the zero degree isotherm (cf. Yala Glacier; Immerzeel et al., 2014). Lapse rates that changed
 2113 depending on season and time of day (given marked monsoonal and nocturnal lowering of lapse rates)
 2114 averaging $5.54 \text{ }^\circ\text{C km}^{-1}$ were calculated and, following integration with the glacier model, produced
 2115 glacier-wide mass balance and spatial calculations that were closest to those from geodetic observations,
 2116 including maximum rates of surface lowering in the upper ablation area where the debris layer is
 2117 thinnest (King et al., 2020) (Fig. 1d).

2119 Analysis of meteorological observations made between 2,600 m and 5,600 m a.s.l. from the Ev-K2-
 2120 CNR and Glacioclim networks indicated that precipitation gradients were weak, slightly negative or
 2121 absent across the Dudh Koshi catchment, confirming the observations of Salerno et al. (2015) and Yang
 2122 et al. (2017). Given the high incidence of missing precipitation data from high-elevation AWS, the
 2123 undercatch of snow associated with tipping bucket rain gauges, and the absence of precipitation
 2124 measurements above 5,600 m a.s.l. precipitation was not varied with elevation. To test the sensitivity
 2125 of precipitation to elevation, COSIPY was forced by a gridded climate distributed using weak negative,
 2126 weak positive, and no precipitation gradients. The results of these experiments were used to force the

Formatted: Font: 11 pt, Not Bold, Font colour: Auto

Formatted: Justified

Formatted: Font: 11 pt

Deleted: ¶

Formatted: Font: Bold

Deleted: 4

Deleted:

Deleted: lapse rates

Deleted: .

Deleted: that variable.

Deleted: . The lapse rates were calculated from meteorological observations, as described below

Deleted: temperature

Deleted: rates

Deleted: $-0.00554 \text{ }^\circ\text{C m}$

Deleted: observed

Deleted: being observed

Formatted: Font: Not Italic

Deleted: lapse rates

2141 glacier model, and the simulated historical glacier evolution was similar, with only a 10 m difference
2142 in the maximum ice thickness between simulations with different precipitation gradients.

2143
2144 Direct solar radiation across the model domain was corrected by the slope, azimuth, and shadowing
2145 potential of each pixel (Wohlfahrt et al., 2016; Sauter et al., 2020). A footprint-weighted correction was
2146 also applied to horizontal measurements of net radiation. The fraction of diffuse incoming shortwave
2147 radiation was estimated by using the ratio of total shortwave (global) radiation and potential shortwave
2148 radiation to define a clearness index (Wohlfahrt et al., 2016). This clearness index was used to calculate
2149 diffuse radiation, which is calibrated with data from Neustift, an eddy covariance station in the Austrian
2150 Alps (Wohlfahrt et al., 2008). The distributed radiative fluxes were compared with high-elevation
2151 stations for 2019 to assess the efficacy of this method across the domain. Pressure was distributed across
2152 the domain by first calculating sea level pressure (*cf.* Lente and Osz, 2020) and then interpolated with
2153 the barometric equation. The relative humidity gradient was calculated as $-0.002\% \text{ m}^{-1}$ from Ev-K2-
2154 CNR and Glacioclim networks and validated with National Geographic network to capture trends at
2155 higher elevations (Matthews et al., 2020). Wind speed was assumed to be uniform across the domain.

2156
2157

2159 **Additional references for Appendix A**

2160 Gupta, A. and Tarboton, D.G. 2016. A tool for downscaling weather data from large-grid reanalysis
2161 products to finer spatial scales for distributed hydrological applications. Environmental
2162 Modelling & Software. 84, pp. 50–69. <https://doi.org/10.1016/j.envsoft.2016.06.014>
2163 Gutmann, E. D., J. J. Hamman, M. P. Clark, T. Eidhammer, A. W. Wood, and J. R. Arnold, 2022: EN-
2164 GARD: A Statistical Downscaling Framework to Produce and Test Large Ensembles of Climate
2165 Projections. J. Hydrometeor., 23, 13545–1561. <https://doi.org/10.1175/JHM-D-21-0142.1>.
2166 Immerzeel, W., Petersen, L., Raegtli, S. and Pellicciotti, F. 2014. The importance of observed gradients
2167 of air temperature and precipitation for modelling runoff from a glacierized watershed in the
2168 Nepalese Himalayas. Water Resources Research. 50: 2212-2226. doi: 10.1002/2013WR014506.
2169 Lente, G. and Osz, K., 2020. Barometric formulas: various derivations and comparisons to
2170 environmentally relevant observations. ChemTexts, 6, pp.1-14. [https://doi.org/10.1007/s40828-](https://doi.org/10.1007/s40828-020-01111-6)
2171 020-01111-6
2172 Li, H., Sheffield, J. and Wood, E.F., 2010. Bias correction of monthly precipitation and temperature
2173 fields from Intergovernmental Panel on Climate Change AR4 models using equidistant quantile
2174 matching. Journal of Geophysical Research: Atmospheres, 115(D10).
2175 <https://doi.org/10.1029/2009JD012882>
2176 Ruane, A. C., Goldberg, R., and Chryssanthacopoulos, J. 2015. Climate forcing datasets for agricultural
2177 modeling: Merged products for gap-filling and historical climate series estimation, Agricultural
2178 and Forest Meteorology, 200, pp. 233–248. <https://doi.org/10.1016/j.agrformet.2014.09.016>
2179 Salerno, F., Guyennon, N., Thakuri, S., Viviano, G., Romano, E., Vuillermoz, E., Cristofanelli, P.,
2180 Stocchi, P., Agrillo, G., Ma, Y., and Tartari, G. (2015). Weak precipitation, warm winters and
2181 springs impact glaciers of south slopes of Mt. Everest (central Himalaya) in the last 2 decades
2182 (1994–2013), The Cryosphere. 9: 1229-1247. doi: 10.5194/tc-9-1229-2015.
2183 Vrac, M., Stein, M.L., Hayhoe, K. and Liang, X.Z., 2007. A general method for validating statistical
2184 downscaling methods under future climate change. Geophysical Research Letters, 34(18).
2185 <https://doi.org/10.1029/2007GL030295>
2186 Wohlfahrt, G., Hammerle, A., Haslwanter, A., Bahn, M., Tappeiner, U. and Cernusca, A. 2008.
2187 Disentangling leaf area and environmental effects on the response of the Net Ecosystem Co2
2188 Exchange to diffuse radiation, Geophysical Research Letters, 35(16).
2189 doi:10.1029/2008gl035090.
2190 Wohlfahrt, G., Hammerle, A., Niedrist, G., Scholz, K., Tomelleri, E. and Zhao, P. 2016. On the energy
2191 balance closure and net radiation in complex terrain, *Agricultural and Forest Meteorology*, 226–
2192 227, pp. 37–49. doi:10.1016/j.agrformet.2016.05.012.
2193 Yang, K., N. Guyennon, L. Ouyang, L. Tian, G. Tartari, and F. Salerno (2017). Impact of summer
2194 monsoon on the elevation-dependence of meteorological variables in the south of Central
2195 Himalaya. International Journal of Climatology. 5293: 1748-1759. doi:10.1002/joc.5293.

Deleted: lapse rates

Deleted: per

Formatted: Font colour: Auto

Moved up [12]: **COSIPY surface energy balance modelling**

balance model that integrates a surface energy and mass balance model with a multi-layer snow and ice model (Weidemann et al.,

Moved up [14]: ¶

Where SW_{in} is incoming shortwave radiation, α is albedo, LW_{in} and LW_{out} are incoming and

Moved up [15]: When T_s exceeds the melting point it is reset to 0°C (273.15 K) and the residual F fluxes equal Q_{melt} . In this instance, subsurface melt is triggered when the energy fluxes, for example, penetrating SW_{in} warm the ice layer so that T_s exceeds the melting point of ice (Sauter et al., 2020). ¶

Moved up [17]: The exchange processes at the surface, including energy release and consumption with phase changes, control temperature distribution and phase changes

Moved up [27]: (a) Locations of energy balance (EB) points

Moved up [19]: Between 5,900–7,900 m a.s.l.,

Moved up [18]: Haut Glacier D’Arolla (Brock et al., 2006).

Deleted: -----Page Break----- (... [14])

Deleted: 2018). It thereby resolves all energy fluxes (... [15])

Deleted: out-going longwave radiation and Q_{sens} , Q_l (... [16])

Deleted: The coupling of the surface energy balance (... [17])

Deleted: BI:

Deleted: EB6480) and (b-f) 5-day average of energy flux (... [18])

Formatted: Font: 10 pt, Not Bold

Formatted: Font: Bold

Formatted: Font: 11 pt

Moved up [22]: α_{firm}

Deleted: QLW sometimes rises above zero during the (... [19])

Deleted: These values were adopted as endmembers of (... [20])

Deleted: $\alpha_{freshsnow}$ (... [21])

Deleted: ¶ (... [22])

Formatted: Font: 11 pt

Formatted: Font: 11 pt

Formatted: Font: 11 pt

Formatted: Font: Not Bold

Formatted: Font colour: Auto

Formatted: Font colour: Auto

Formatted (... [23])

Deleted: Brock, B.W., Willis, I.C. and Sharp, M.J., (... [24])

Formatted: Font colour: Auto

Deleted: Irvine-Fynn, T.D., Sanz-Ablanedo, E., Rut (... [25])

Deleted: Luo, M., Liu, T., Meng, F., Duan, Y., Frank (... [26])

Deleted: Stoc-¶ (... [27])

Page 5: [1] Deleted	Ann Rowan	21/10/2025 12:14:00
---------------------	-----------	---------------------

▼

Page 5: [1] Deleted	Ann Rowan	21/10/2025 12:14:00
---------------------	-----------	---------------------

▼

Page 5: [1] Deleted	Ann Rowan	21/10/2025 12:14:00
---------------------	-----------	---------------------

▼

Page 5: [1] Deleted	Ann Rowan	21/10/2025 12:14:00
---------------------	-----------	---------------------

▼

Page 5: [2] Deleted	Ann Rowan	21/10/2025 12:14:00
---------------------	-----------	---------------------

▼

Page 5: [2] Deleted	Ann Rowan	21/10/2025 12:14:00
---------------------	-----------	---------------------

▼

Page 5: [2] Deleted	Ann Rowan	21/10/2025 12:14:00
---------------------	-----------	---------------------

▼

Page 5: [2] Deleted	Ann Rowan	21/10/2025 12:14:00
---------------------	-----------	---------------------

▼

Page 5: [2] Deleted	Ann Rowan	21/10/2025 12:14:00
---------------------	-----------	---------------------

▼

Page 5: [2] Deleted	Ann Rowan	21/10/2025 12:14:00
---------------------	-----------	---------------------

▼

Page 5: [2] Deleted	Ann Rowan	21/10/2025 12:14:00
---------------------	-----------	---------------------

▼

Page 5: [3] Deleted	Ann Rowan	21/10/2025 12:14:00
---------------------	-----------	---------------------

▼

Page 5: [4] Deleted	Ann Rowan	21/10/2025 12:14:00
---------------------	-----------	---------------------

▼

Page 5: [5] Deleted	Ann Rowan	21/10/2025 12:14:00
---------------------	-----------	---------------------

▼

Page 5: [6] Deleted	Ann Rowan	21/10/2025 12:14:00
---------------------	-----------	---------------------

▼

Page 5: [6] Deleted	Ann Rowan	21/10/2025 12:14:00
---------------------	-----------	---------------------

▼

Page 5: [7] Formatted	Ann Rowan	21/10/2025 12:14:00
-----------------------	-----------	---------------------

Font colour: Auto

Page 5: [7] Formatted	Ann Rowan	21/10/2025 12:14:00
-----------------------	-----------	---------------------

Font colour: Auto

Page 5: [7] Formatted	Ann Rowan	21/10/2025 12:14:00
-----------------------	-----------	---------------------

Font colour: Auto

Page 5: [8] Formatted	Ann Rowan	21/10/2025 12:14:00
-----------------------	-----------	---------------------

Font colour: Auto

Page 5: [8] Formatted	Ann Rowan	21/10/2025 12:14:00
-----------------------	-----------	---------------------

Font colour: Auto

Page 5: [9] Formatted	Ann Rowan	21/10/2025 12:14:00
-----------------------	-----------	---------------------

Left, Add space between paragraphs of the same style

Page 7: [10] Deleted	Ann Rowan	21/10/2025 12:14:00
----------------------	-----------	---------------------

▼

Page 7: [11] Deleted	Ann Rowan	21/10/2025 12:14:00
----------------------	-----------	---------------------

▼

Page 7: [12] Deleted	Ann Rowan	21/10/2025 12:14:00
----------------------	-----------	---------------------

▼

Page 32: [13] Deleted	Ann Rowan	21/10/2025 12:14:00
-----------------------	-----------	---------------------

▼

Page 37: [14] Deleted	Ann Rowan	21/10/2025 12:14:00
-----------------------	-----------	---------------------

▼

Page 37: [15] Deleted	Ann Rowan	21/10/2025 12:14:00
-----------------------	-----------	---------------------

▼

Page 37: [16] Deleted	Ann Rowan	21/10/2025 12:14:00
-----------------------	-----------	---------------------

▼

Page 37: [17] Deleted	Ann Rowan	21/10/2025 12:14:00
-----------------------	-----------	---------------------

▼

Page 37: [18] Deleted	Ann Rowan	21/10/2025 12:14:00
-----------------------	-----------	---------------------

▼

Page 37: [19] Deleted	Ann Rowan	21/10/2025 12:14:00
-----------------------	-----------	---------------------

▼

Page 37: [20] Deleted	Ann Rowan	21/10/2025 12:14:00
-----------------------	-----------	---------------------

▼

Page 37: [21] Deleted	Ann Rowan	21/10/2025 12:14:00
-----------------------	-----------	---------------------

▼

Page 37: [22] Deleted	Ann Rowan	21/10/2025 12:14:00
-----------------------	-----------	---------------------

▼

Page 37: [23] Formatted	Ann Rowan	21/10/2025 12:14:00
-------------------------	-----------	---------------------

Font: 10 pt, Font colour: Auto, Not Highlight, Ligatures: Standard + Contextual

Page 37: [24] Deleted	Ann Rowan	21/10/2025 12:14:00
-----------------------	-----------	---------------------

▼

Page 37: [25] Deleted	Ann Rowan	21/10/2025 12:14:00
-----------------------	-----------	---------------------

▼

Page 37: [26] Deleted	Ann Rowan	21/10/2025 12:14:00
-----------------------	-----------	---------------------

▼

Page 37: [27] Deleted	Ann Rowan	21/10/2025 12:14:00
-----------------------	-----------	---------------------

▼